Acta Materialia 189 (2020) 10–24

Contents lists available at ScienceDirect

Acta Materialia

journal homepage: www.elsevier.com/locate/actamat

Full length article

Metallic glass instability induced by the continuous dislocation absorption at an amorphous/crystalline interface

Thanh Phan[a], Ji Rigelesaiyin[a], Youping Chen[b], Ashraf Bastawros[a,c,d,e], Liming Xiong*[,a]

[a] Department of Aerospace Engineering, Iowa State University, Ames, Iowa 50011, USA
[b] Department of Mechanical and Aerospace Engineering, University of Florida, Gainesville, FL 32611, USA
[c] Department of Mechanical Engineering, Iowa State University, Ames, Iowa 50011, USA
[d] Department of Material Science and Engineering, Iowa State University, Ames, Iowa 50011, USA
[e] Ames Laboratory, Division of Materials Science and Engineering, Ames, Iowa 50011, USA

ARTICLE INFO

Article History:
Received 23 September 2019
Revised 15 February 2020
Accepted 16 February 2020
Available online 29 February 2020

Keywords:
Dislocation
Shear transformation zone
Effective temperature
Molecular dynamics
Multiscale simulations
Amorphous-crystalline metallic composites

ABSTRACT

An amorphous/crystalline metallic composite (A/C-MC) integrates metallic glass with crystalline metals in one system. The amorphous-crystalline interface (ACI) in A/C-MCs under deformation absorbs dislocations and may fundamentally change the dilemma that the strength comes at the expense of the ductility of a material. However, the development of such materials is still at a trial and error stage due to the lack of a clear-cut understanding on how the amorphous component become instable when a dislocation-mediated plasticity flows into the glassy phases. To meet this need, here we focus on gaining the physical insights into the dislocation-ACI reaction in A/C-MCs through atomistic simulations. We have **(i)** digitally resembled an interface structure close to that in experiments by annealing melted metallic glasses at cooling rates as low as $\sim 10^4$ K/s; **(ii)** correlated the dislocation absorption events with the activation of shear transformation zones (STZs) in A/C-MCs under a plastic shear; **(iii)** identified the mechanisms responsible for a continuous dislocation absorption-induced instability in glassy phases; **(iv)** calibrated a set of constitutive relations, kinetic rules, and model parameters that can be used in an effective temperature concept-based STZ theories at the continuum level; and **(v)** characterized the local stress states ahead of the instability band and lay the macroscopic-level glass instability criterion on a firm atomistic basis. Our major findings are: **(a)** there exists a nanoscale structure transition at the ACI when the cooling rate in the atomistic simulations is reduced to an experimentally-comparable level; **(b)** the number of atoms participating in the STZs exponentially increases with the number of dislocations arriving at the ACI at an early stage of the dislocation-ACI reaction, but is linearly proportional to the number of absorbed dislocations at a later stage; **(c)** the dislocation absorption-induced instability in metallic glasses occurs through a three-stage process, i.e., the activation of STZs in the region between icosahedral (ICO) clusters, the coalescence of newly formed STZs, and then the breakdown of ICOs; **(d)** the model parameters in the continuum-level constitutive relations and kinetic rules are found to be sensitive to cooling rates; and **(e)** the local stress states ahead of the instability band in glassy phases map surprisingly well with the Mohr-Coulomb criterion regardless of the applied stress at the macroscopic level. The gained knowledge may provide a pathway of connecting the atomistic deformation physics of an A/C-MC with its overall mechanical performance, which is currently difficult to achieve in laboratory experiments.

1. Introductions

In the search of strong and ductile materials, one strategy is introducing interfaces, such as grain boundaries (GBs) [1–4], twin boundaries [5–7], or phase boundaries [8–11], to resist dislocation motions. This strategy is always accompanied by a decrease in material ductility although it does lead to a significant enhancement in material strength [1–11]. In contrast, instead of blocking dislocations, inspired by the nature of biological materials such as nacre [12] and dental enamel [13], an amorphous/crystalline metallic composite (A/C-MC), which combines amorphous metallic glasses with crystalline metals [14–16], introduces the amorphous-crystalline interfaces (ACIs) to absorb dislocations. It has a potential to significantly expand the strength-ductility envelope by facilitating a co-deformation near the ACIs. For instance, a simultaneous high-strength and high-ductility [14–16] was recently realized in a typical A/C-MC, Cu/CuZr [14–16]. However, a rational design of such materials is not achieved

* Corresponding author.
E-mail address: lmxiong@iastate.edu (L. Xiong).

https://doi.org/10.1016/j.actamat.2020.02.038
1359-6454/

yet due to the lack of a well-established microstructure-property relationship. Correlating the complex material [15,16] microstructure of an A/C-MC with its overall performance is not trivial because its deformation mechanism is complicated and remains largely unclear. The complexity of its mechanical behavior, especially the plastic deformation, stems from the coupled dynamics between two distinct plasticity carriers: dislocations carry the plasticity in metallic crystals while the STZs, which comprise a local shear among a small cluster containing $\sim$10–50 atoms, act as the plasticity carriers in metallic glasses. When plasticity flows from the crystalline into the amorphous phases, dislocations hit the ACIs and activate STZs. This may lead to the instability of a glassy phase by initiating a shear band. Clearly, in order to establish the interrelationship between the microstructure, deformation physics, and the overall performance of an A/C-MC, as a first step, the interplay between dislocations and STZs needs to be characterized from the bottom up.

In the past decades, extensive experiments [15,17–22] have been conducted to examine the deformation behavior of A/C-MCs. One pioneering work using the transmission electron microscopy demonstrated that the ACIs in A/C-MCs act as a high-capacity sink of dislocations [15]. Later on, using a high-resolution transmission electron microscopy (HRTEM), Zhang and his co-workers [17–22] revealed that the absorbed dislocations not only activated the STZs, but also crystallized the amorphous phases. Recently, through a combined atom probe tomography and HRTEM analysis [22], a dislocation absorption-induced mechanical alloying was also observed. Despite these compelling experimental observations, there exists, however, no commonly agreed explanation for the co-deformation of crystalline and amorphous phases. One reason is that, the mechanistic insights were mainly extracted from the post-mortem analysis in experiments. Due to the extremely short time scales and the very small length scales, an in situ experimental study of the deformation processes at a buried ACI in A/C-MCs remains difficult, if not impossible. Fortunately, experiments can be always supplemented with high-fidelity computer simulations. Especially, many current computer simulation tools may be applicable to examine the spatiotemporal correlation between dislocations and STZs in an A/C-MC on the fly of its deformation.

Historically, computer models at the continuum level have enjoyed the most popularity for understanding how plasticity flows in materials. They concern the macroscopic-level material behavior at a length scale which is much larger than the characteristic size of a plasticity carrier. As far as the A/C-MCs are concerned, a typical continuum model requires (i) constitutive relations and kinetic rules for describing the continuous dislocation absorption-induced plasticity in metallic glasses; and (ii) a local strain- or stress-controlled criterion for detecting a dislocation absorption-induced instability. In addition, due to the limited resolution, the continuum-level computer model, e.g., a diffuse-interface model [23] or a phase field model [24], for an A/C-MC always homogenizes the material interface as an intermediate phase with a uniform thickness, modulus, and strength in a phenomenological manner. The above two requirements of the continuum computer models yield their limited power in predicting the deformation behavior of A/C-MCs, unless the rules for describing the dislocation-ACI interactions are calibrated from a finer scale experiments or simulations.

This has motivated a large amount of molecular dynamics (MD) simulations [25–29] of A/C-MCs with a variety of aims to (a) describe its interface structure at an atomistic resolution [25]; (b) construct its deformation mechanism map at the nanoscale [26]; and (c) quantify the dependence of its properties on the chemical composition and microstructures [27]. Although these MD simulations have largely advanced the understanding of the deformation behavior in A/C-MCs, a gap between atomistic, experiments, and continuum-level models still exists because: (1) there is a significant difference between the cooling rates in simulated (10^9 K/s or above) and real (10^6 K/s or below) glassy phases; (2) the information required by a continuum model, i.e., the kinetic rules for the interplay between dislocations and STZs, as well as the criterion for detecting the onset of a dislocation absorption-induced instability, is missing. This in turn, leads to a series of unanswered questions: how does the short- and medium-range order (SRO and MRO) configure in an amorphous phase when the atomistic model is prepared at an experimentally-comparable cooling rate? How will the SRO-MRO structures compromise with the long-range order (LRO) of the adjacent crystals in A/C-MCs? How does the microstructure of an amorphous phase evolve with the continuous dislocation absorption at the ACI? What is the correlation between the rate of STZ formation and the number of the absorbed dislocations? Whether the instability of a glassy phase in an A/C-MC occurs under the same conditions as that in a bulk glassy phase? What is the local stress state ahead of a continuous dislocation absorption, and how is it related with the Mohr–Coulomb criterion [30,31]? Can the Mohr-Coulomb criterion, which is widely used for the bulk metallic glass instability, be applicable to predict the localized plastic events in A/C-MCs under deformation? If so, on what length scales?

With an attempt of answering these questions, the rest of this paper is organized as follows: in Section 2, we introduce the chosen materials and the set-up of the computer models, including the boundary conditions, the sample dimensions, as well as the interatomic force fields. In order to simulate a continuous dislocation absorption-induced instability in metallic glasses, a loading strategy of driving a sequence of dislocations to interact with an ACI at the same site is introduced. Section 3 presents the simulation results. It mainly includes: (i) the cooling rate dependence of the material microstructure; (ii) the three-stage deformation processes responsible for the dislocation absorption-induced plastic flow in A/C-MCs; (iii) the quantitative correlation between the number of dislocations absorbed by an ACI and the number of atoms participating the STZs; (iv) the calibration of constitutive relations and kinetic rules to be used as inputs for describing the plasticity of metallic glasses in the effective temperature concept-based STZ theories; (v) the atomistic stress measurement ahead of the tip of a shear instability using the Virial [32,33] and also a recently developed mechanical stress formula [34–36]; and (vi) the calibration of a criterion that can be used for detecting a dislocation absorption-induced instability in metallic glasses. Section 4 summarizes the major finding of this work. The limitations of the present simulations as well as the relevant future research endeavor along this direction is also discussed.

2. Simulation details

In this work, Cu/CuZr is chosen as a model material because: (a) CuZr-based A/C-MCs exhibit a combined high-strength and high-ductility [15–22,25–29], making these alloys promising in engineering applications; (b) Cu_xZr_{1-x} has a good glass-forming ability and is an ideal system for computational studies because a wide range of compositions ($0.2 < x < 0.7$) can be made amorphous [37,38]; (c) interatomic force fields, including Finnis–Sinclair [39,40] and embedded atom method (EAM) [40–43] potentials, are all well-developed and readily to be used in MD simulations of glassy CuZr; and (d) extensive HRTEM experiments have been conducted to examine the structure change in a deformed Cu/CuZr [15–22], which provides information for cross-validating the computational results. All of these factors make the Cu/CuZr a good prototype for understanding how plastic deformation occurs in A/C-MCs at a fundamental level.

Fig. 1 a shows the computational set-up for simulating the dislocation-ACI reactions in a bi-layered $Cu/Cu_{64}Zr_{36}$. This atomistic model combines a 90 nm-thick Cu with a 20 nm-thick $Cu_{64}Zr_{36}$ layer. Here the Cu and $Cu_{64}Zr_{36}$ layer thickness are set to be 90 nm and 20 nm, respectively, because: (i) a typical thickness ratio between Cu and CuZr layers in the multilayered Cu/CuZr composites with an

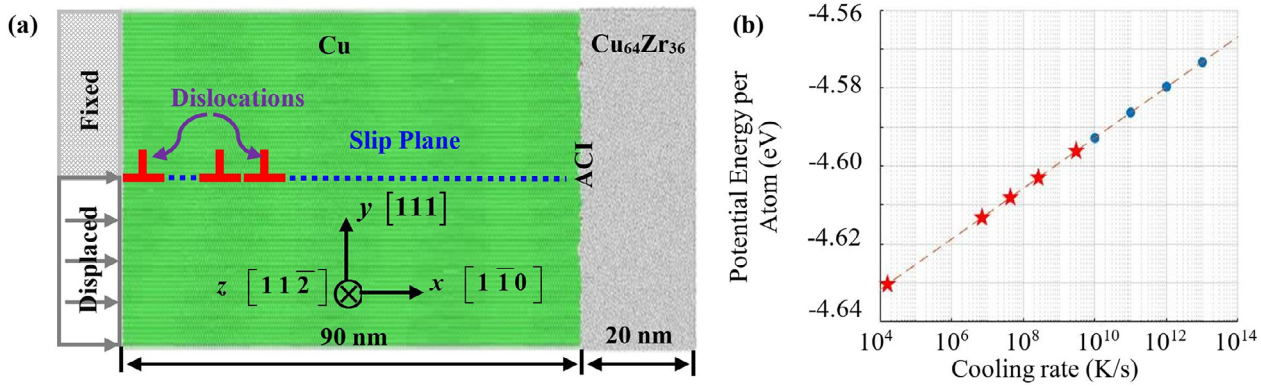

Fig. 1. Atomistic simulation of the dislocation-ACI reaction in a bi-layered Cu/$Cu_{64}Zr_{36}$: (a) the computational set-up; (b) potential energy of the $Cu_{64}Zr_{36}$ as a function of the cooling rates before its combination with the Cu layer. The red stars represent effective cooling rates from the sub-T_g annealing. (For interpretation of the references to colour in this figure legend, the reader is referred to the web version of this article.)

exceptional property [15] is found to be around 7:1; (ii) the primary focus of this work is to investigate how the instability in $Cu_{64}Zr_{36}$ occurs when it absorbs a sequential of dislocations at the same site of an ACI; (iii) the Cu layer thickness needs to be sufficiently large for accommodating such a number of dislocations, which are separated at an equilibrium spacing of $\sim$10 nm between each other; and (iv) the dislocations will be injected into the model at the free end of the Cu layer using an indenter, which introduces a high local stress there. A set-up of Cu layer thickness at 90 nm may effectively reduce this local stress-induced pollution on the dislocation-ACI reaction mechanism. The sample is computationally prepared through three stages: (1) generate a small glassy $Cu_{64}Zr_{36}$ cubic cell containing $\sim$10, 000 atoms by quenching it from the melting to 1 K; (2) construct a rectangular $Cu_{64}Zr_{36}$ sample with a dimension of $110 \times 10 \times 20$ nm^3 by replicating the small glassy cubic cell along x, y, and z directions. By this way, an atomistic model of one $Cu_{64}Zr_{36}$ layer containing $\sim 3.4 \times 10^5$ atoms is built; (3) combine the annealed $Cu_{64}Zr_{36}$ with a crystalline Cu slab (crystallographic orientation is shown in Fig. 1a). Thereafter, the bi-layered Cu/$Cu_{64}Zr_{36}$ simulation cell enclosing $\sim$2 million atoms is equilibrated for another $\sim$200 ps. The quenching and equilibration are performed in an isothermal-isobaric ensemble under zero external stress, as implemented in LAMMPS [44,45]. The time-step is set to be 2 fs. A classical EAM potential [40] that satisfactorily describes the glass microstructures of a CuZr system is used. The temperature is controlled using the Nose-Hoover thermostat algorithm [33]. The sample is set to be finite along the x and y directions but periodic along the z direction. Followed by the equilibration, a sequence of dislocations (Fig. 1a) is introduced. Each dislocation has a Burgers vector of $\mathbf{b} = \frac{a_0}{2}[110]$. They are generated by fixing one half of the Cu layer on the top left edge of the sample while rigidly displacing the other half on the bottom left edge (Fig. 1a). In details, in order to nucleate one single dislocation, the bottom left edge of the sample is displaced by $b_S = a_0 \frac{\sqrt{6}}{6}$ along the $[2\bar{1}1]$ direction and then followed by a displacement of $b_S = a_0 \frac{\sqrt{6}}{6}$ along the $[1\bar{2}\bar{1}]$ direction. By this way, each dislocation is in a full edge type but disassociates into a leading and a trailing partial. Thereafter, the rigidly displaced atoms on the bottom left edge of the sample remain to be fixed. Meanwhile, a constant shear stress of $\tau_{xy} = 0.5$ GPa is imposed to drive the dislocation migration towards the Cu/CuZr interface. Such a procedure is repeated until 40 dislocations are injected, each of which is followed by a relaxation period of 60 ps. This loading strategy is effective for unraveling the mechanisms of a continuous dislocation-ACI reaction at the same site in A/C-MCs.

In order to map an atomistic simulation-revealed mechanism to the overall performance of Cu/$Cu_{64}Zr_{36}$ characterized in experiments, as a first step, the amorphous $Cu_{64}Zr_{36}$ in the computer model needs to be prepared at an experimentally-comparable cooling rate (10^6 K/s or even below). Different from many existing MD simulations which use ultrahigh cooling rate (10^9 K/s or above) [25–29], here we achieve the low cooling rates using a sub-T_g algorithm [46–48]. The fundamental principle underlying the sub-T_g algorithm is: (i) when the system temperature, T, is well above the glass-transition temperature, T_g, an amorphous phase can be relaxed within picoseconds. In this temperature regime, a fast cooling rate of 10^{10} K/s or above is sufficient; and (ii) when $T \ll T_g$, the experimentally-observed ultra-slow physical aging of an amorphous material is beyond the reach of atomistic cooling rates but can be accessible through numerical annealing. In this work, using the sub-T_g algorithm, before combining it with Cu, a fully equilibrated amorphous $Cu_{64}Zr_{36}$ is obtained through: (1) melting the $Cu_{64}Zr_{36}$ at 2000 K; (2) cooling the melted $Cu_{64}Zr_{36}$ at a constant rate of 10^{10} K/s to slightly below its glass-transition temperature, $\sim$700 – 800 K, in 120 ns; and then (3) annealing the sample isothermally for 300 ns and bringing it to a low temperature in another 80 ns until the potential energy per atom in the $Cu_{64}Zr_{36}$ system is –4.615 eV. According to the extrapolation of a linear relationship between the atomic potential energy and the cooling rate (Fig. 1b), this atomic-level potential energy corresponds to an effective cooling rate of $\sim 10^6$ K/s. The annealing in step-3 can be further extended towards an even lower potential energy for achieving an effective cooling rate as low as $\sim 10^4$ K/s. As demonstrated in [46], comparing with many conventional atomistic simulations, the simulated microstructure of CuZr system prepared through such a sub-T_g annealing procedure can resemble the realistic microstructure of metallic glasses observed in experiments.

3. Results

3.1. Cooling rate-dependent atomic packing and interface structure

To investigate the cooling rate dependence of the microstructure in Cu/CuZr, we prepare $Cu_{64}Zr_{36}$ under five different cooling rates: 10^{13} K/s, 10^{11} K/s, 10^9 K/s, 10^6 K/s, and 10^4 K/s. Its local atomic packing is characterized using the Voronoi tessellation method [42,43,49–52]. The Voronoi tessellation is a widely-used tool for determining the atomic packing in glassy materials. It divides a space into many polyhedrons, each of which is associated with an atom, and is built through constructing the bisecting planes along the lines joining the atom and all its neighbors. For each atom, its Voronoi polyhedra cell will be noted as an index notation, $\langle n_3, n_4, n_5, n_6 \rangle$, where n_i stands for the number of faces with i edges in the Voronoi polyhedra. The sum of n_i is the coordination number of the centered atom. For instance, $\langle 0, 2, 6, 4 \rangle$ refers a polyhedron bounded by 2 quadrangles, 6 pentagons, and 4 hexagons. The coordination number of the atom with such a Voronoi index will be 12. By this notation,

one typical SRO in metallic glasses is a collection of the atoms with a Voronoi index of ⟨0, 0, 12, 0⟩, which is usually referred as a full icosahedra (ICO). The centered atom in an ICO bonds with 12 neighbors. Such ICOs were found to have a configurational energy of 8.4% lower than that of a dense-packed f.c.c. or h.c.p. cluster [46,53]. They form MROs through interpenetrating with each other. Those MROs are believed to be the backbone of a metallic glass for resisting the mechanical deformation [42,43].

Fig. 2 a shows the atomic-level configurations of the ICOs at a cross-section in $Cu_{64}Zr_{36}$ prepared at 10^{13} K/s, 10^{11} K/s, 10^{6} K/s, and 10^{4} K/s, respectively. In Fig. 2a, each ICO is represented by a sphere and only the centered atoms are displayed. The spheres are colored according to how each ICO shares a volume with its neighbors to different degrees. Here we would like to clarify that, to estimate the fraction of ICOs, only those Cu-centered ICOs which carry a Voronoi index of ⟨0, 0, 12, 0⟩ are counted. In other words, only the red atoms in Fig. 2a contribute to the fraction of ICOs presented in Fig. 2b. Those blue atoms surrounding the red ones in Fig. 2a are not counted during the estimation of the fraction of ICOs. Under this condition, the snapshots of the ICO configurations in Fig. 2a are seen to be consistent with its fraction estimation in Fig. 2b. A cooling rate dependence of the ICO configuration can be clearly seen here: (i) the ICOs in $Cu_{64}Zr_{36}$ obtained at high cooling rates, e.g., 10^{11} K/s and above, are low in population and isolated from each other; (ii) under the intermediate cooling rates ranging from 10^{8} K/s to 10^{10} K/s, they tend to connect with each other and form strings, most of which are short in length and spatially uncorrelated; and **(iii)** when the cooling rates are as low as 10^{6} K/s or below, a large amount of ICOs fall into the cut-off distance of their neighbors and organize as interpenetrating networks. Clearly, when the cooling rates are reduced from 10^{13} K/s to 10^{4} K/s, there exists a microstructure transition from the isolated ICO clusters to the ICO strings, and then to the cross-linked ICO networks in $Cu_{64}Zr_{36}$. This result suggests that the reduction of a cooling rate enables the system to arrive at lower energy states towards a more comfortable atomic packing.

In Fig. 2b, the fraction of the ICOs, f_{ico}, is plotted as a function of the cooling rate, c. Here the f_{ico} is calculated as the ratio between the number of atoms acting as the ICO centers (the red spheres in Fig. 2a) and the total number of the atoms in the system. Fig. 2b shows that f_{ico} dramatically climbs from ~7% to ~40% when the cooling rate, C, changes from 10^{13} K/s to 10^{4} K/s. In parallel to the cooling rate-dependent ICO configurations as shown in Fig. 2a, Fig. 2b demonstrates that the f_{ico} - C relation is linear but piece wised: **(i)** when the cooling rate is reduced from 10^{13} K/s to 10^{10} K/s, f_{ico} increases from ~8% to ~15%, which corresponds to the connections of isolated ICOs and the formations of strings; **(ii)** when the cooling rates are in the range between 10^{8} K/s and 10^{4} K/s, those newly formed ICO strings cross link with each other and develop the three-dimensional ICO networks. At this stage, f_{ico} increases from ~25% to ~40%; and **(iii)** in between, i.e., when the cooling rates range from 10^{10} K/s to 10^{8} K/s, f_{ico} changes from ~15% to ~25%. Based on the above results, we believe that, for a metallic glass prepared under a wide range of cooling rates, its atomic packing should not be simply considered to be linearly proportional the cooling rates as suggested in [54]. Instead, the ICO configurations are formed through distinct mechanisms when the cooling rate falls into different regimes. In the later sections of this paper, it is demonstrated that the varieties of the ICO configurations in $Cu_{64}Zr_{36}$ prepared under different cooling rates leads to distinct kinetics on how they absorb the incoming dislocations. Despite of that, it should be noticed that there exists a scatter about the cooling rate dependence of the ICO fraction in the literature. Particularly, in atomistic simulations, many aspects of the computer model, such as the chemical composition, the interatomic force field, the sample size, the boundary conditions, and of course, the strategies of estimating the fraction of ICOs, may affect the atomistic simulation-predicted ICO density and distribution. Nevertheless, our finding in Fig. 2b agrees well with the pioneering research results in [54], where the fraction of Cu-centered ICOs with a Voronoi index of ⟨0, 0, 12, 0⟩ were found to increase from 0.28 to 0.48 when the cooling rate is reduced from 10^{13} K/s to 10^{10} K/s. As such, we believe our observations in the Fig. 2b are qualitatively reasonable, although a quantitative experimental evidence is still in need for validation.

When combined with Cu, the $Cu_{64}Zr_{36}$ layer will be under a topological constraint imposed by the abutting Cu crystals. The cooling rate-dependent ICO configurations in the $Cu_{64}Zr_{36}$ layer will in turn, give rise to a variety of interface structures in $Cu/Cu_{64}Zr_{36}$. Fig. 3 presents the atomic configuration together with its atomic density profiles across the ACIs in $Cu/Cu_{64}Zr_{36}$ prepared under 10^{11} K/s (Fig. 3a) and 10^{6} K/s (Fig. 3b), respectively. Here the atomic density is measured by uniformly partitioning the simulation box along the x direction into bins, each of which has a finite volume of $V_i = D_x \times L_y \times L_z$. As suggested by Brandl and his co-workers in [55], the local atomic density in each bin (D_x = 0.03 nm) is calculated as $q(x) = N(x)/(D_x \times L_y \times L_z)$, where L_y and L_z are the dimensions of the sample along the y and z directions. The atomic density profiles in Fig. 3a and b can be divided into three characteristic regimes: (1) in

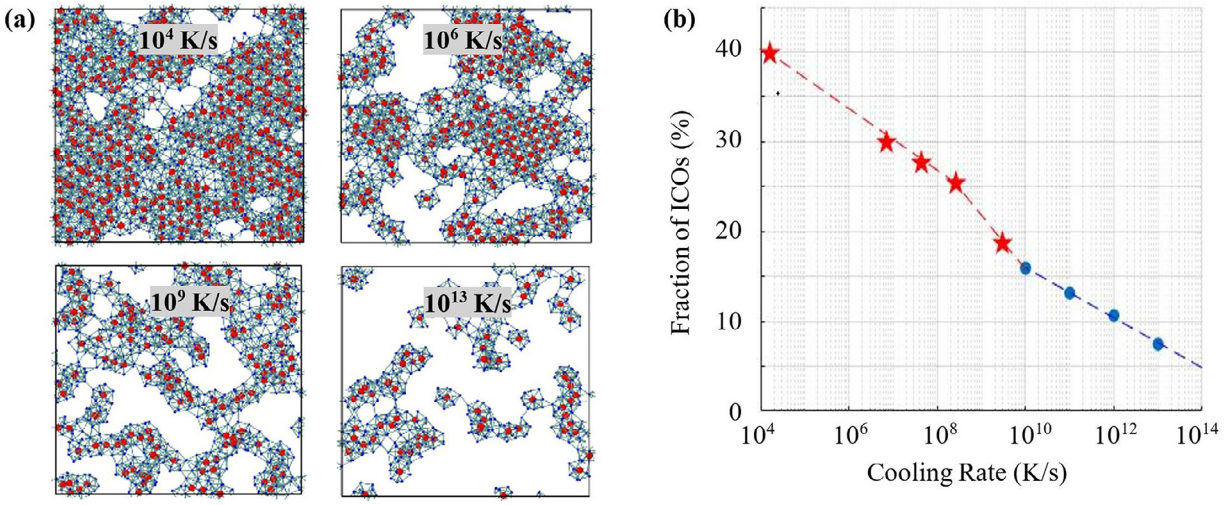

Fig. 2. The cooling rate-dependent microstructures in $Cu_{64}Zr_{36}$: (a) the atomistic configurations of the ICOs at a cross-section of the $Cu_{64}Zr_{36}$ formed under a wide range of cooling rates ranging from 10^{13} K/s to 10^{4} K/s; (b) the population of ICOs as a function of the cooling rates. The red stars represent the effective cooling rates from the sub-T_g annealing. (For interpretation of the references to colour in this figure legend, the reader is referred to the web version of this article.)

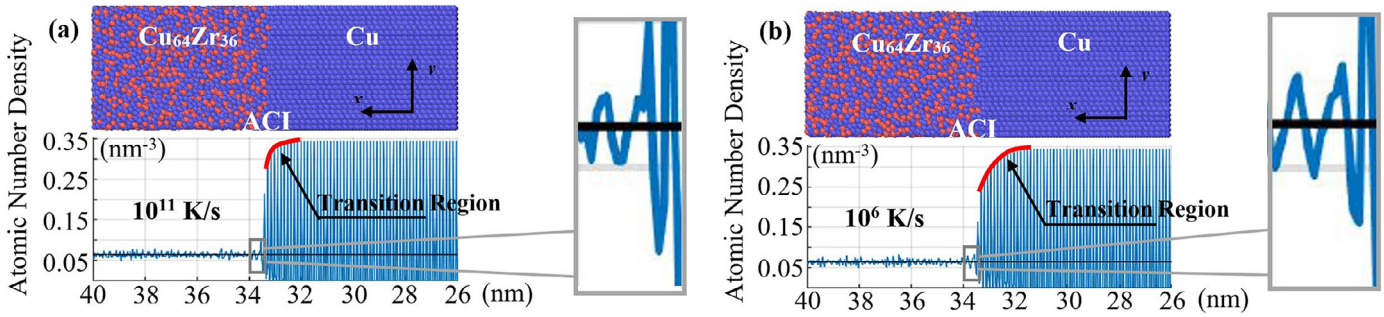

Fig. 3. The structure and the atomic number density profile near an interface in bi-layered Cu/$Cu_{64}Zr_{36}$ prepared under two typical different cooling rates: (a) 10^{11} K/s; (b) 10^{6} K/s.

the crystalline Cu domain far away from the ACI, the periodic pattern appears. This pattern reflects the stacking of the atomic planes in f.c.c. Cu; (2) in a finite-width transition region (indicated by the red curves in Fig. 3a, b) nearby the ACIs, the atomic density peaks broaden and the magnitude of those peaks decrease. This implies an increase of the atomic spacing as well as the structure disorder; and (3) when the amorphous $Cu_{64}Zr_{36}$ is approached, those sharp peaks are fully broad (the inset pictures in Fig. 3a, b) and oscillate around a constant value approximately. Quantitatively, similar to a previous result in [55], Fig. 3 shows that the atomic number density in a Cu layer is nearly 6 times that of amorphous $Cu_{64}Zr_{36}$. This, of course, does not simply imply there exists such a huge mass density difference between Cu and $Cu_{64}Zr_{36}$ because the atomic masses of Cu and Zr has not been included into the formula of $q(x)$. If the atomic masses are included, a distribution with a comparable mass density between Cu and $Cu_{64}Zr_{36}$ should be expected. Also, under the current definition of $q(x)$, the difference between the atomic number density in Cu and $Cu_{64}Zr_{36}$ is actually not a constant, and will depend on the bin size of D_x. We found that the atomic number density difference between Cu and $Cu_{64}Zr_{36}$ can be significantly reduced if $D_x = 0.06$ nm is used. However, no matter which D_x is used, a transition region (red curves) between Cu and $Cu_{64}Zr_{36}$ can be always identified, a structural and chemical gradient is formed across the ACI. Such a transition region has a measurable extent and is obviously necessary for bridging the long-range-order in Cu with the SRO and MRO in amorphous $Cu_{64}Zr_{36}$. This region is relatively sharp and spans only ~ 1 nm when the cooling rates are 10^{11} K/s (Fig. 3a), but has an island structure spanning ~ 2 nm when the cooling rate is 10^{6} K/s (Fig. 3b). Such a cooling rate-dependent interface structure can be rationalized as a consequence of Zr migrations from the amorphous $Cu_{64}Zr_{36}$ into the crystalline Cu phase when the sample is cooled from melting to a low temperature. The results in Fig. 3 suggest that lowering the cooling rates may bring a smoother interface structure transition in Cu/$Cu_{64}Zr_{36}$. This is believed to be closer to a real laboratory process at a long-time scale limit, where a migration of Zr into the Cu layer occurs indeed. Therefore, although our atomistic simulation here precludes any long-range diffusional processes due to its limited timescales, it still shows the possibility of manipulating the ACI structure in A/C-MCs through a fine control of the cooling rates during the sample preparation.

3.2. Deformation mechanisms for the interplay between dislocations and STZs

When the Cu/$Cu_{64}Zr_{36}$ sample is under a plastic shear, its deformation behavior will be fundamentally dictated by the synergetic coupling between dislocations and STZs. To understand how the glassy phase accommodates the strain heterogeneities brought by the incoming dislocations, in this section, we provide the atomistic details of the dislocation-ACI reactions. We analyze the plastic flow in Cu/$Cu_{64}Zr_{36}$ prepared under two cooling rates (10^{11} K/s in Fig. 4a and 10^{6} K/s in Fig. 4b). Fig. 4a, b show the atomic von Mises strain together with the ICO configuration evolution in Cu/$Cu_{64}Zr_{36}$ under shear. Here the von Mises strain is extracted from the atomic Green–Lagrangian strain tensor [56,57]. It

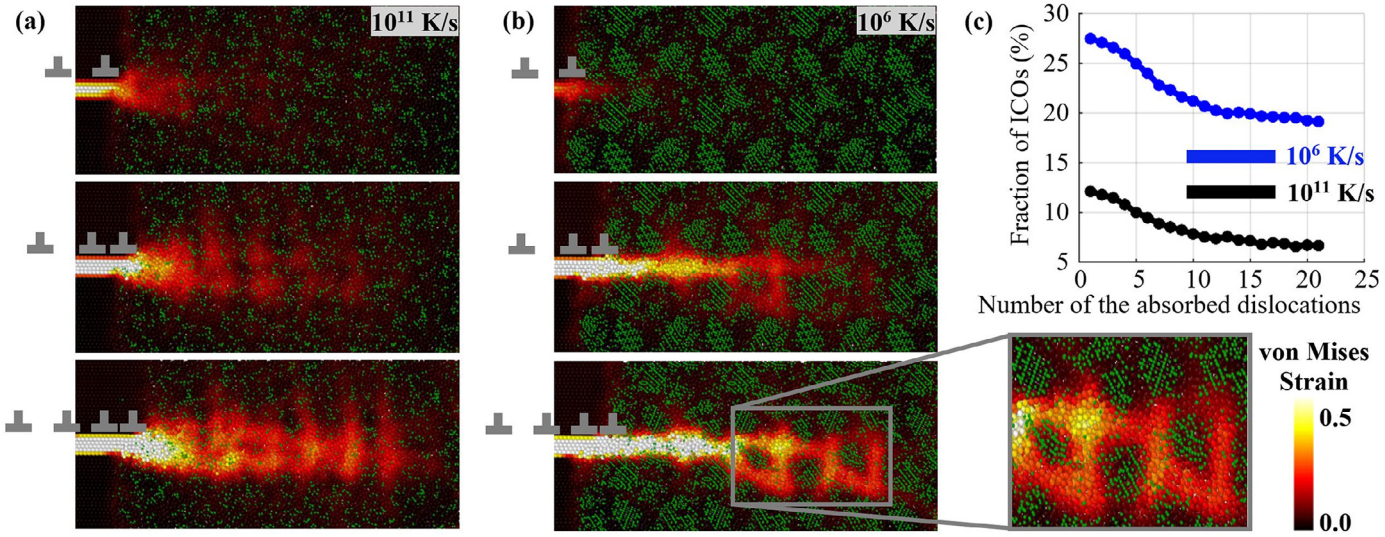

Fig. 4. Snapshots from the atomistic simulations of the co-deformation of the crystalline and amorphous phases in bi-layered Cu/$Cu_{64}Zr_{36}$ prepared under a cooling rate of (a) 10^{11} K/s and (b) 10^{6} K/s; (c) the correlation between the fraction of the atoms participating the ICOs in $Cu_{64}Zr_{36}$ and the number of the absorbed dislocations at the ACIs.

is based on the deformation gradient as a least-square fit to the atomic displacement vectors. The strain calculated in this way reflects the topology change of the atomic clusters in materials under deformation. The color scale in Fig. 4a, b indicates that the local von Mises strain ranging from 0.0 to 0.5 when the number of the dislocations arriving at the ACI increases from 0 to 22.

Meanwhile, in order to visualize the microstructure evolution in $Cu_{64}Zr_{36}$, the ICO centers (green particles in Fig. 4a, b) are also tracked. The time sequences of the snapshots in Fig. 4a, b demonstrate that, when dislocations are absorbed at the ACI, the $Cu_{64}Zr_{36}$ deform through a three-stage process: **(i)** at the early stage, when the first $2 \sim 3$ dislocations arrive at the ACI, a few atomic clusters in the $Cu_{64}Zr_{36}$ near the dislocation-ACI intersection experience an elevated strain at a level of ~ 0.2 or above, indicating an onset of STZs without breaking the ICOs in $Cu_{64}Zr_{36}$. The plastic strain brought by the incoming dislocations diffuses into the glassy phases by activating STZs in âæsoft spotsâg. These soft spots are the polyhedra located in between the ICOs. They usually have the most uncomfortable topological and chemical environments, such as the polyhedra with Voronoi indices ⟨0, 3, 6, 2⟩, ⟨0, 4, 4, 3⟩, and ⟨0, 2, 8, 3⟩, etc. In order to accommodate the dislocation-mediated slip transfer across the ACI, those soft spots serve as fertile sites for STZ activations. The distribution of STZs at this stage is discontinuous and separated by the ICOs. It is believed that, the newly formed STZs in between the ICOs can promote the nucleation of other STZs in the surrounding soft spots through an autocatalytic process as suggested in [58,59]; (ii) when the number of dislocations arriving at the ACI increases up to 5, we still do not see a significant change in the ICO configuration. Rather, we observe a coalescence of those newly formed STZs. It implies that, at this stage, the ICO networks remain the elastic backbone of the glassy phases. The STZs connect with each other to carry the deformation by forming a channel of plastic flow; (iii) upon a further loading, tens of dislocations are absorbed by the $Cu_{64}Zr_{36}$. At this moment, the ICO skeleton in $Cu_{64}Zr_{36}$, cannot bear the accumulated strain and starts to be broken.

To further confirm the above three-stage deformation process, in Fig. 4c, we plot the fraction of the atoms participating the ICOs as a function of the number of the absorbed dislocations, N_{dis}. Here, we only monitor the ICO fraction evolution in a finite-sized region, rather than the whole amorphous $Cu_{64}Zr_{36}$ layer. This region is located ahead of the dislocation-ACI intersection. The width of this region is 1/4 of the whole amorphous layer thickness, which corresponds to the saturated shear band width as listed in the third column of Table. 1. During the dislocation absorption, the ICO configuration out of this domain remains mostly unchanged, and are thus omitted. Fig. 4c shows that: **(a)** the fraction of ICOs slightly changes when $N_{dis} < 5$; and **(b)** the ICO fraction drops dramatically (from $\sim 25\%$ to $\sim 20\%$ in $Cu_{64}Zr_{36}$ prepared at 10^6 K/s and from $\sim 10\%$ to $\sim 7\%$ in $Cu_{64}Zr_{36}$ prepared at 10^{11} K/s) when N_{dis} increases from 5 to 15. The destruction of ICOs results in the increased population of the compliant disordered clusters. This leads to the strain accumulation along a preferential direction (Fig. 4a, b). Correspondingly, the atomic von Mises strain in $Cu_{64}Zr_{36}$ organizes into a localization band which follows the direction of the dislocation-mediated slip in Cu. Along this band, the strain is localized and considerably high. The profile gradually becomes smooth comparing with the discontinuous strain distribution at the early stage of the deformation. A further plastic flow is then carried by the propagation of this strain localization band. Eventually, an offset, which shears the upper part of the material with respect to the bottom part, is formed across the entire sample. In addition, a comparison between Fig. 4a, b shows that, under the same plastic shear, the deformation in Cu/$Cu_{64}Zr_{36}$ prepared at 10^6 K/s (Fig. 4b) is carried by a narrower band. Within this band, the strain concentration is more severe than that in the sample prepared at 10^{11} K/s. It suggests that the capacity and efficiency of $Cu_{64}Zr_{36}$ in absorbing dislocations are sensitive to its microstructure. The glasses prepared at a lower cooling rate contains more ICOs and exhibits a stronger propensity in activating STZs, which form a more localized band. We envision that this result may find applications in supporting the development of ductile A/C-MC with a fine control of its microstructure through tuning its thermal processing history. However, we are also fully aware that, due to the limited length scales, the present atomistic model does not reproduce the full-scale material microstructure evolution, which actually spans from nanometers to micrometers and even above.

Table 1
The STZ-PF model parameters fitted from atomistic data and the standard deviation (R^2) during the fitting procedure. Dimensionless lengths are normalized by the $Cu_{64}Zr_{36}$ layer thickness L.

Cooling Rates	$\mathcal{L}/L$	w_∞/L	R^2
10^6 K/s	0.1798	0.1549	0.935
10^{10} K/s	0.4242	0.2370	0.980
10^{11} K/s	0.5657	0.2541	0.932
10^{12} K/s	1.0575	0.3722	0.984

Based on the above atomistic simulations, the number of the atoms participating STZs in $Cu_{64}Zr_{36}$ can be correlated with the number of the absorbed dislocations (Fig. 5a). Fig. 5a shows that such a correlation can be divided into three characteristic stages: (i) at stage-I, when the number of dislocations arriving at the ACI, noted as N_{dis}, is less than five, the number of the atoms participating STZs, N_{STZ}, exponentially increases with N_{dis}. At this stage, STZs mainly nucleate in the soft regions around the ICOs; (ii) at stage-II, when $5 < N_{dis} < 15$, the STZ coalescence occurs; and **(iii)** at stage-III, when $N_{dis} > 15$, a shear band forms and starts to thicken. At this stage, N_{STZ} is almost linearly proportional to N_{dis}. Also, the slope of the relationship between N_{STZ} and N_{dis} at this stage is found to be sensitive to the cooling rates: the higher the cooling rates, the larger the slope.

The present atomistic simulations can be also used to calibrate the continuum-level kinetic rules, such as the formulation [60–62] based on a thermodynamic criterion for the interactions between plasticity and phase transformation in multiphase materials or the shear-transformation-zone pulled front (STZ-PF) model [63] for the shear band broadening in metallic glasses under deformation. Particularly, in an STZ-PF model, the width of a shear band, w, in a deformed metallic glass is related with the applied shear strain, γ, through [63]

$$-\left(2+\frac{w}{w_\infty}\right)\sqrt{1-\frac{w}{w_\infty}}+\left(2+\frac{w_0}{w_\infty}\right)\sqrt{1-\frac{w_0}{w_\infty}}=\frac{3}{4}\frac{\mathcal{L}L}{w_\infty^2}(\gamma-\gamma_0), \qquad (1)$$

where w_0 and γ_0 are the initial width of a mature shear band and the critical shear strain at which a mature shear band starts to be formed, respectively. The two parameters $\mathcal{L}$, and w_∞, are the instantaneous shear band length and the saturated band width, respectively.

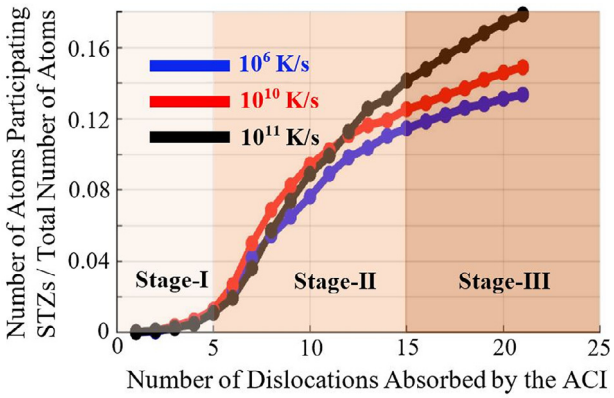

Fig. 5. The atomistic-simulation-predicted correlation between the number of the absorbed dislocations and the fraction of the atoms participating the STZs in the whole amorphous layer.

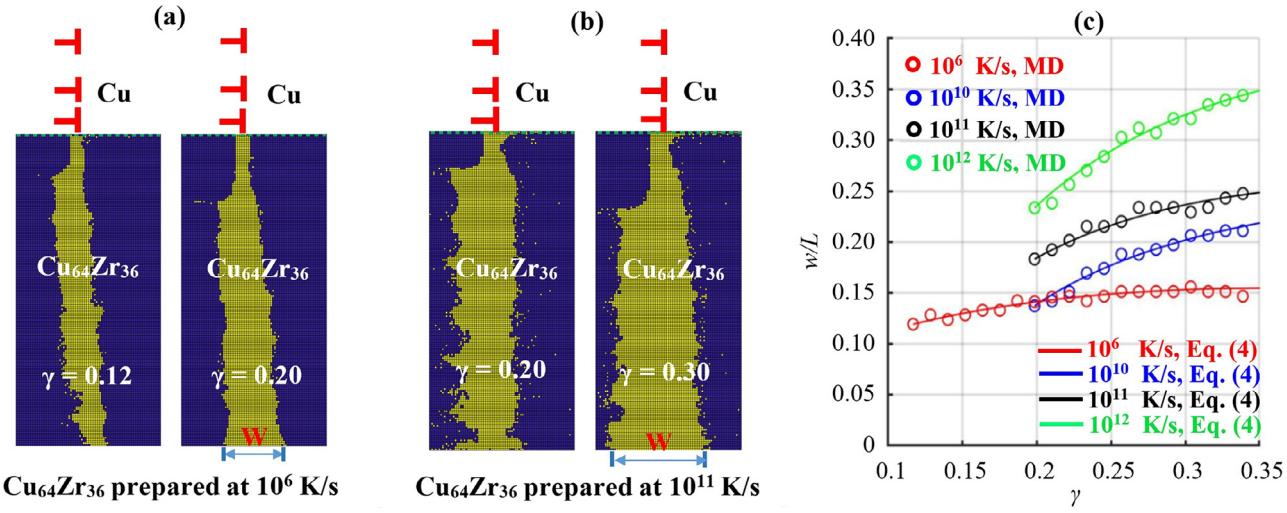

Fig. 6. Informing the atomistic data into the kinetic rules at the continuum level: (a) the snapshots of the shear band (yellow in color) morphology evolution during the dislocation absorption into the $Cu_{64}Zr_{36}$ prepared at 10^6 K/s; and (b) 10^{11} K/s; (c) the atomistic-simulation-data based relation between the applied shear strain, γ, and the normalized width, w/L, for describing the shear band broadening in $Cu_{64}Zr_{36}$ prepared at a variety of different cooling rates. (For interpretation of the references to colour in this figure legend, the reader is referred to the web version of this article.)

Here we demonstrate how the obtained atomistic data can be used to calibrate these two parameters. In details, γ_0 is chosen to be the critical shear strain, which corresponds to a certain number of dislocation absorption when a shear band cutting through the whole $Cu_{64}Zr_{36}$ layer is formed (Fig. 6a, b). Thereafter, upon the continuous dislocation absorption, we monitor the change of the shear band width, w, and plot it as a function of the dislocation absorption-induced shear, γ. Fig. 6c shows that the shear band broadening in $Cu_{64}Zr_{36}$ prepared at different cooling rates significantly differ from each other. Firstly, a significantly lower critical shear ($\gamma_0 = 0.12$) is required to form the shear band in $Cu_{64}Zr_{36}$ prepared at 10^6 K/s than that ($\gamma_0 = 0.2$) required by the sample prepared at 10^{10} K/s or above (Fig. 6c). It means that, comparing with the sample prepared at high cooling rates, the formation of a shear band in a sample prepared at low cooling rates starts earlier. Secondly, the width of a shear band in the sample prepared at 10^6 K/s saturates soon but w almost linearly increases with the increase of γ in $Cu_{64}Zr_{36}$ prepared at high cooling rates (Fig. 6c). Thirdly, for $\gamma > 0.2$, at the same level of shear strain, the width of the shear band in $Cu_{64}Zr_{36}$ is proportional to the cooling rates. For instance, when $\gamma = 0.3$, the normalized shear band widths in $Cu_{64}Zr_{36}$ prepared at 10^6 K/s, 10^{10} K/s, 10^{11} K/s, and 10^{12} K/s are 0.15, 0.20, 0.24, and 0.32, respectively. One important finding here is: the dislocation absorption-induced shear band broadening in $Cu_{64}Zr_{36}$ is sensitive to the cooling rates used in the sample preparations. Such a cooling rate dependent kinetics can be incorporated into the model parameters through fitting the atomistic data to Eq. (1). The values of $\mathcal{L}$ and w_∞ obtained through the data-fitting in Fig. 6c is summarized in the following Table 1.

3.3. Informing the atomistic data into a continuum-level STZ theory

3.3.1. Measurement of the effective temperature

For further scaling up in length, a connection between the present atomistic simulation and a continuum-level STZ theory, especially the one based on the effective temperature concept which enjoys the most popularity in understanding the STZ-mediated plastic flow in amorphous materials, becomes necessary. The main idea of the effective temperature concept-based STZ theory is to describe the deformation of amorphous materials as the evolution of an effective temperature field,which is a dimensionless scalar noted as χ and follows the definition in [62–66]

$$\chi = \frac{k_B}{E_z}\frac{\partial U_c}{\partial S_c}, \tag{2}$$

where k_B is the Boltzmann factor, E_z is the STZ formation energy, U_c and S_c are the material's potential energy and entropy, respectively. For measuring the effective temperature of the amorphous phase from atomistic simulations, a coarse-graining strategy described in [67] is deployed here. In details, the domain of the amorphous phase is placed on a two-dimensional grid. The effective temperature on each grid point, χ, is calculated as [67]

$$\chi = \beta\frac{\sum_{i=1}^{n} g_i\left(E_i - E^0 - E^{el}\right)}{\sum_{i=1}^{n} g_i}, \tag{3}$$

where β is a material specific constant with a unit of the inverse potential energy per atom, n is the number of the atoms neighboring with the grid point under consideration, E_i is the current potential energy of the ith atom. E^0 is the reference energy taken as the average potential energy per atom of the bulk amorphous as obtained in Fig. 1b; the elastic-strain energy, E^{el}, is calculated from the linear-elastic strain energy $E^{el} = \frac{\sigma_{xy}^2}{2E_a}$, where E_a is the Young modulus of bulk amorphous, g_i is the Gaussian function used to weight the contribution of the ith atom in the neighbor list of a grid point and follows a form as [67]

$$g_i = \frac{2}{\sqrt{2\pi}c}\exp\left(-\frac{r_i^2}{2c^2}\right). \tag{4}$$

Here, r_i indicates the distance between the continuum point and the ith atom within a cutoff range of r_{cut}; c is the parameter that determines the width of g_i. According to the previous atomistic simulations [67], χ converges when $r_{cut} > 3c$and $d \le 0.25c$ where d is the spacing between continuum points. Thus, in this work, we choose c = 32 Å, d = 8 Å, and r_{cut} =96 Å.

Starting from Eq. (3), we measure the effective temperature in our atomistic simulations using two different set-ups for β: (i) in one set-up, β is considered to be a constant of 6.1 as suggested in [67]; and (ii) in the other, the cooling rate dependence of β is included, which follows a form as

$$\beta = 2.14 + 3.0\times10^{-7}\left(\ln\left(\frac{C}{C_0}\right)\right)^6, \tag{5}$$

where C is the cooling rate used for preparing the amorphous phases, $C_0 = 10^4$ K/s, which is a cooling rate commonly used in experiments. Using these two different set-up for β, the initial effective temperature distribution and its evolution during the continuous dislocation absorption into the amorphous phases prepared at various cooling rates are presented in Fig. 7. Clearly, if a constant value of β is chosen for measuring the effective temperature, the curves in Fig. 7a, b show a trend of the higher cooling rate, the lower initial effective temperature, and the thicker shear band width. This not only contradicts the a commonly agreed intuition for amorphous materials: the higher cooling rate, the more configurational disorder, and the higher initial effective temperature, but also is inconsistent with the STZ theory-based prediction [68,69] the lower initial effective temperature, the thinner shear band. Such an inconsistency motivates us to develop a new formula for re-defining the effective temperature from the atomistic simulations. The key idea of this new formula is to explicitly consider β as a function of the cooling rate, as shown in Eq. (5), rather than a constant. Surprisingly, using this new formula, we found that the correlation between cooling rate, effective temperature, and shear band thickness (as shown in Fig. 7a, b) can be reversed. That is, as shown in Fig. 7d–e, a lower initial effective temperature is observed in the sample prepared at a lower cooling rate, which results in a thinner shear band after deformation. As such, we suggest that, when connecting the atomistic simulation with a continuum-level STZ theory becomes a purpose, a great care needs to be taken on how the effective temperature should be defined and measured using the atomistic data. For instance, our preliminary practice here has clearly shown that the key parameter, β, used in the effective temperature measurement should be different for amorphous materials prepared at different cooling rates. The physical implications of such a cooling rate dependent β are: (i) the specific heat of the amorphous glasses prepared at different cooling rates will differ from each other because β is with an unit of inverse potential energy per atom and is directly related to the specific heat of an amorphous material [67]; (ii) the STZ formation energy, E_z, is a decreasing function of the increasing cooling rate, i.e., the higher cooling rate, the lower E_z. In details, the values of E_z are found to be 0.47 eV and 1.24 eV in the samples prepared at 10^{11} K/s and 10^6 K/s, respectively. Here, E_z was estimated from $E_z = k_B T_g / \chi_\infty$. In this equation, k_B is the Boltzman constant, T_g is equal to 760 K and is the glassy transition temperature, χ_∞ is the steady state effective temperature (the values of χ_∞ are 0.138 and 0.053 for the samples prepared at 10^{11} K/s and 10^6 K/s, respectively) extracted from Fig. 7d where a cooling rate-dependent β has been used; and (iii) an incorporation of the cooling rate dependence into the effective temperature measurement from atomistic simulations may enable the STZ theory to capture a full range of experimentally observed behavior, such as the cooling rate-dependent aging, steady-state flow, and serrated-to-nonserrated transition, in glassy materials under deformation.

3.3.2. Calibration of the STZ transformation rate

In order to predict the micro-structure evolution in A/C-MCs under deformation at the macroscopic level, there is a need to inform the above dislocation absorption-induced STZ dynamics into the

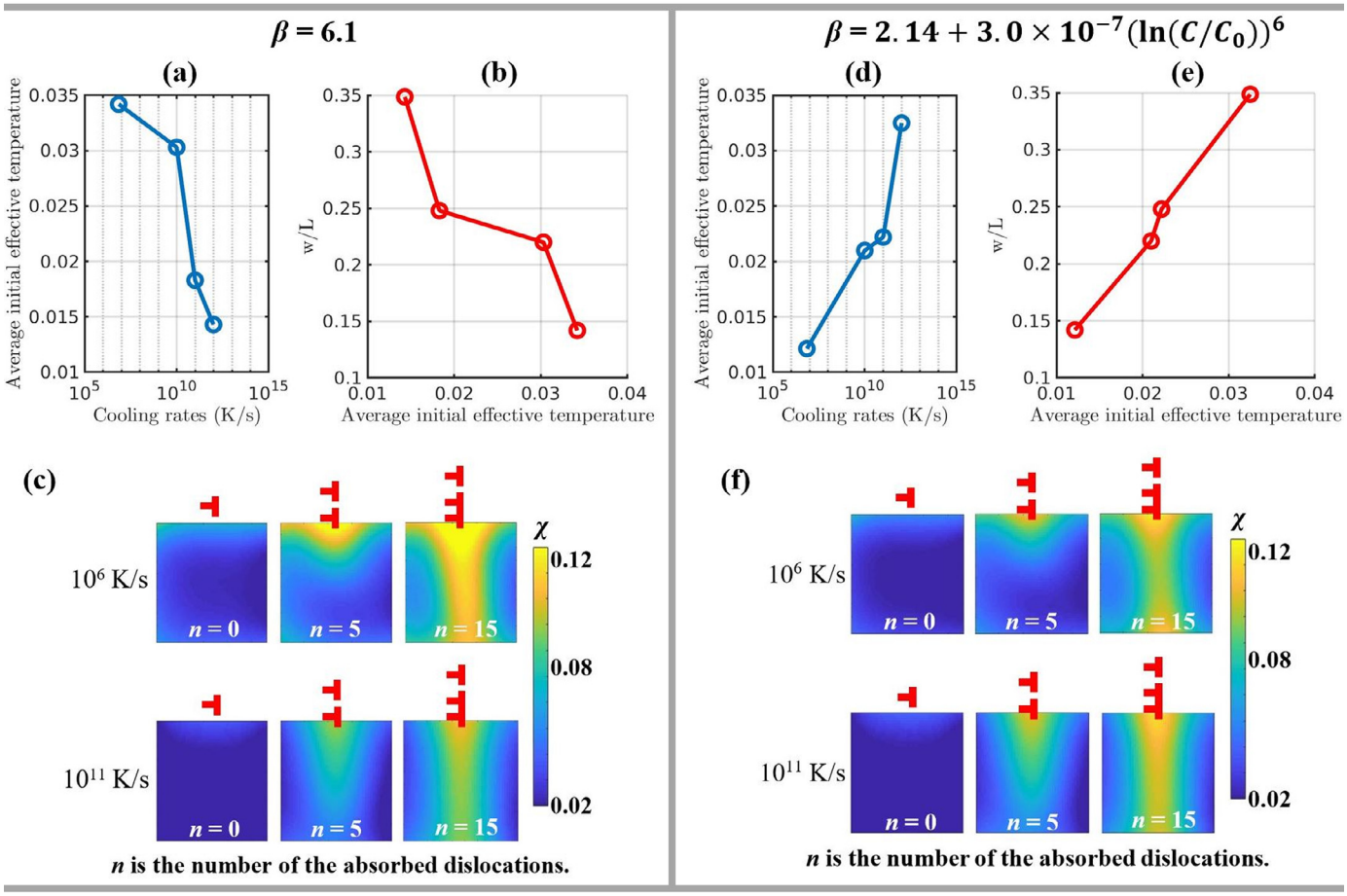

Fig. 7. A direct measurement of the effective temperature in amorphous phases from atomistic simulations using constant value of β (a–c) and a cooling rate-dependent β (d–f). The correlation between the initial effective temperature and the cooling rates is shown in (a) and (d). The correlation between the initial effective temeprature and the saturated shear band thickness is shown in (b) and (e). The effective temperature evolution during the continuous dislocation absorption into the amorphous phases prepared at two different cooling rates is shown in (c) and (f). The shear band width/length, w/L, in (b) and (e) is extracted from Fig. 6c, not measured from the effective temperature distribution in (c) and (f).

continuum-level theories or computer models, such as the crystal plasticity [23], phase field [24], or the STZ theory [67,70]. These models, especially the STZ theories, describe the plastic flow in amorphous materials using constitutive relations and kinetic rules. For example, in one recent work [67], the plastic deformation rate, $\dot{\epsilon}^{pl}_{xy}$, of an amorphous solid subjected to a shear within the xy plane is related with the local shear stress, σ_{xy}, through a constitutive relation

$$\tau_0 \dot{\epsilon}^{pl}_{xy} = \exp\left(\frac{-1}{\chi}\right) f(\sigma_{xy}), \tag{6}$$

where τ_0 is the atomic time scale and is taken to be 10^{-15} s, f is the transformation rate and is a function of the local stress, σ_{xy}. An analytical form of f has been proposed in [70]

$$f(\sigma_{xy}) = \cosh\left(\frac{\epsilon_0 \sigma_{xy} a^3}{\chi}\right)\left(\tanh\left(\frac{\epsilon_0 \sigma_{xy} a^3}{\chi}\right) - \frac{\sigma_0}{\sigma_{xy}}\right), \tag{7}$$

where a is the atomic radius, σ_0 is a controlling parameter, and is related to the material's yielding stress, σ_y, through the following relation [70]

$$\sigma_0 = \sigma_y \tanh\left(\frac{\epsilon_0 \sigma_y a^3}{\chi}\right). \tag{8}$$

Due to its crucial role in the STZ theory, a careful calibration of f from fine-scale simulations or high-resolution experiments is necessary. However, a direct experimental measurement of the transformation rate and the local stress in glassy phases under deformation remains not trivial. By contrast, the atomistic-simulation-predicted relation between N_{STZ} and N_{dis} in Fig. 5 provides us with an opportunity to calibrate $f(\sigma_{xy})$ from the bottom up. In details, firstly, the number of dislocations, N_{dis}, is converted to the plastic deformation rate, $\dot{\epsilon}^{pl}_{xy}$, on the fly of the simulations. Secondly, upon the arrival and the absorption of each dislocation, at a material point ahead of the instability band in $Cu_{64}Zr_{36}$, we measure not only the local stress, σ_{xy}, but also the local effective temperature, χ.χ associated with that material point is calculated using the newly developed Eq. (3)for β. at the atomic level.

Combining Eqs. (3), (4), and (6), the value of $f(\sigma_{xy})$ at the material point ahead of the instability band can be determined on the fly of the continuous dislocation absorption in $Cu_{64}Zr_{36}$. Fig. 8 presents the relevant results for $Cu_{64}Zr_{36}$ prepared under a cooling rate of 10^6 K/s and 10^{11} K/s, respectively. For comparison, the analytical form of $f(\sigma_{xy})$ in Eq. (7) is also included. Fig. 8 clearly shows that the atomistic simulation-based $f(s)$ is zero below a critical stress but is nonzero above. An incorporation of this finding into Eq. (6) will naturally lead to the STZ theory-predicted bifurcation behavior of an amorphous material: the plastic strain rate is zero below a critical stress, and nonzero above. This critical stress is noted as the yield stress of the amorphous phases, and is found to be 1.8 GPa for $Cu_{64}Zr_{36}$ when it is prepared at a cooling rate of 10^6 K/s, and is 1.2 GPa when prepared at 10^{11} K/s. Combining the knowledge of "the lower cooling rate, the lower initial effective temperature" gained in Fig. 7d–f, here we confirm a previous STZ theory-based prediction [64,65]: the amorphous material's yield stress is a decreasing function of the increasing effective temperature. If this yield stress is noted as σ_y, then the single parameter, σ_0, which controls the amorphous material's bifurcation behavior can be calculated using Eq. (8). It should be noticed that, in Figure. 8, there exists not only a similarity but also a difference between atomistic data and the analytical form of $f(\sigma_{xy})$. Especially, when local stress level is high, the atomistic data starts to diverge from the analytical form. This may imply that the current analytical form is inadequate to fully describe the local STZ activities and requires a further calibration. Also, in Fig. 8, we clearly see that, when the local shear stress level is beyond the yield stress, $f(\sigma_{xy})$ in the sample prepared at a high cooling rate (Fig. 8b) increases significantly faster and eventually arrives at a much higher magnitude than that in the amorphous phase prepared at a lower cooling rate (Fig. 8a). Such a cooling rate-dependent $f(\sigma_{xy})$ in Fig. 8 is believed to originate from the distinct material microstructure between those two samples.

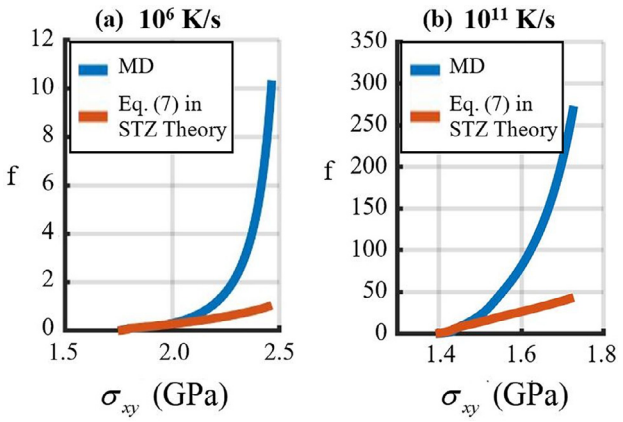

Fig. 8. The analytical form, Eq. (7), and its comparison with the atomistic simulation-based $f(\sigma_{xy})$ which may be used as an input in the constitutive relation of a continuum-level STZ theory for describing the plastic flow in $Cu_{64}Zr_{36}$ prepared at (a) 10^6 K/s; and (b) 10^{11} K/s.

Fig. 8 provides us with a strategy of measuring the local yield stress, σ_y, at one material point ahead of the dislocation-ACI intersection. In the same manner, the yield stress at a series of material points away from the interface can be also characterized. Its distribution as a function of the distance away from the interface is plotted in Fig. 9. Clearly, no matter the amorphous phase is prepared at a low cooling rate of 10^6 K/s or a high cooling rate of 10^{11} K/s, our atomistic simulations agree with an STZ theory-based finding [70]: the amorphous material is weaker near the ACI. Moreover, the atomistic data obtained here can be used to calibrate the material model in [70]. Similar to Eq. (45) in [70], here we propose a mathematical expression as following to describe the change of the material's yielding stress as a function of the distance away from the ACI:

$$\frac{\sigma_y(x)}{E_a} = p_1 - e^{p_2 + p_3 x} \tag{9}$$

where x is the distance away from the interface in angstroms, p_1, p_2, and p_3 are the model parameters, and E_a is the Young's modulus of the amorphous phase.Comparing with the Eq. (45) in [70], Eq. (9) is more general because it not only reasonably describes the local yielding stress as a function of the distance away from the ACI, but also incorporates the cooling rate dependence of a local yielding into the model parameters of p_1, p_2, and p_3. The values of them can be obtained through fitting the atomistic data into Eq. (9), and are summarized in the Table 2.

3.3.3. *Calibrating the effective temperature diffusion coefficient and bridging atomistic to continuum*

In addition to its usage in calibrating the shear transformation rate, the atomistic simulation-based effective temperature evolution can be also used to extract a so-called effective temperature diffusion coefficient, noted as D. This parameter can be fed into a diffusion equation in STZ theories to describe the plastic deformation of the amorphous phase in an amorphous/crystalline metallic composites under deformation [70].

Table 2
The p_1, p_2, and p_3 parameters in Eq. (9) fitted from the atomistic data in Fig. 9.

Cooling Rates	p_1	p_2	p_3
10^6 K/s	0.060	−3.734	−1.305
10^{11} K/s	0.058	−3.415	−2.005

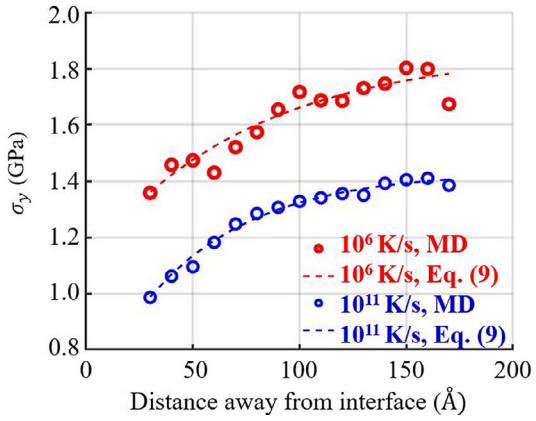

Fig. 9. The local yield stress, σ_y, of the amorphous phase as a function of distance away from the interface. The circles indicate the atomistic data, and the dash lines are obtained through fitting the atomistic data into Eq. (9).

$$\left(\frac{d\chi}{dt}\right)_{\text{diff}} = Da^2\dot{\epsilon}^{pl}\frac{\partial^2\chi}{\partial x^2}, \tag{10}$$

where D is the effective temperature diffusion constant, a is the atomic diameter, and x is the dimension orthogonal to the interface. Our atomistic data shows that the effective temperature diffusion coefficient, D, is cooling rate dependent, rather than a constant. The values of D are found to be 5000 and 20,000 in the amorphous$Cu_{64}Zr_{36}$ prepared at cooling rates of 10^6 K/s and 10^{11} K/s, respectively. Using these atomistic simulation-based diffusion constants as inputs, Eq. (10) can be numerically solved. During the continuous dislocation absorption into the amorphous phases under an applied shear strain, the effective temperature distribution as a function of the distance away from the interface is obtained. The results are plotted in Fig. 10 and agree well with that from the fully atomistic simulations. A comparison between Fig. 10a and b also shows that the effective temperature diffuses significantly more slowly in $Cu_{64}Zr_{36}$ prepared at a low cooling rate than it does in a fast-cooled sample. This is physically reasonable and provides us with confidence on informing the atomistic data into the continuum-level computer models for simulating the plastic deformation behavior in amorphous materials or relevant composites using the effective temperature concept-based STZ theories.

To briefly summarize Section 3.3, a series of atomistic simulation-informed constitutive relations and kinetic rules, which take into account of the effects of cooling rates on the deformation behavior in glassy phases, are calibrated here. They can be then informed into the STZ theory. This may in turn, enable the prediction of the microstructure evolution in a plastically deformed A/C-MCs at the continuum level, if supplemented with a criterion for detecting the dislocation absorption-induced instability, which is believed to be controlled by the local stress states and is discussed in the following two sections.

3.4. Local stress state ahead of the dislocation-absorption-induced instability in metallic glasses

In this section, we analyze the local stress field ahead of a continuous dislocation absorption-induced instability in metallic glasses using the atomic Virial stress [32,33] described in Eq. (11) and the direct mechanical stress definition expressed in Eq. (12)

$$\boldsymbol{\sigma}^{\text{Pot}}_{\text{Virial}}(\boldsymbol{x}) = \frac{1}{V}\left\langle \sum_{k,l}\boldsymbol{F}_{kl}\boldsymbol{r}_{kl}\right\rangle, \tag{11}$$

$$\boldsymbol{\sigma}^{\alpha\beta}_{\text{Mechanical}}(\boldsymbol{x}) = \frac{1}{2}\sum_{k,l}\int_{L_{kl}} F^{\alpha}_{kl}\bar{\delta}^{\beta}_{A}(\phi-\boldsymbol{x})d\phi\boldsymbol{e}^{\alpha}\boldsymbol{e}^{\beta}, \tag{12}$$

where $\boldsymbol{F}_{kl}$ and $\boldsymbol{r}_{kl}$ are interaction force and separation distance between atoms k and l, and $\bar{\delta}^{\beta}_{A}(\phi-\boldsymbol{x})$ is the averaged Dirac delta over a surface element with area A. The normal direction of this area is noted as β.

Although the Virial stress formula has been widely used in MD to measure the local stress in an atomistic system, recently both analytical and numerical works [34–36] have shown that the Virial stress formula is distinct from Cauchy stress, and does not satisfy momentum conservation law [64,65]. The Cauchy stress measures the force *per unit area*, whereas the Virial formula, the potential part of which is given in Eq. (11), calculates the product of interatomic forces and distances, i.e., $\boldsymbol{F}_{kl}\boldsymbol{r}_{kl}$, *per unit volume*. This distinction suggests that the Virial formula may not be appropriate for measuring the local stress in inhomogeneous materials, which has been intensively discussed in [66,71,72]. A formula different from the Virial stress was derived by Chen and her co-workers [34–36] using a formalism that extends the Irving-Kirkwood procedure in deriving microscopic fluxes as ensemble averaged point functions [73–75] to instantaneous quantities. This formula was proved to recover the continuum definition of Cauchy stress at the atomic scale and satisfy the conservation laws.

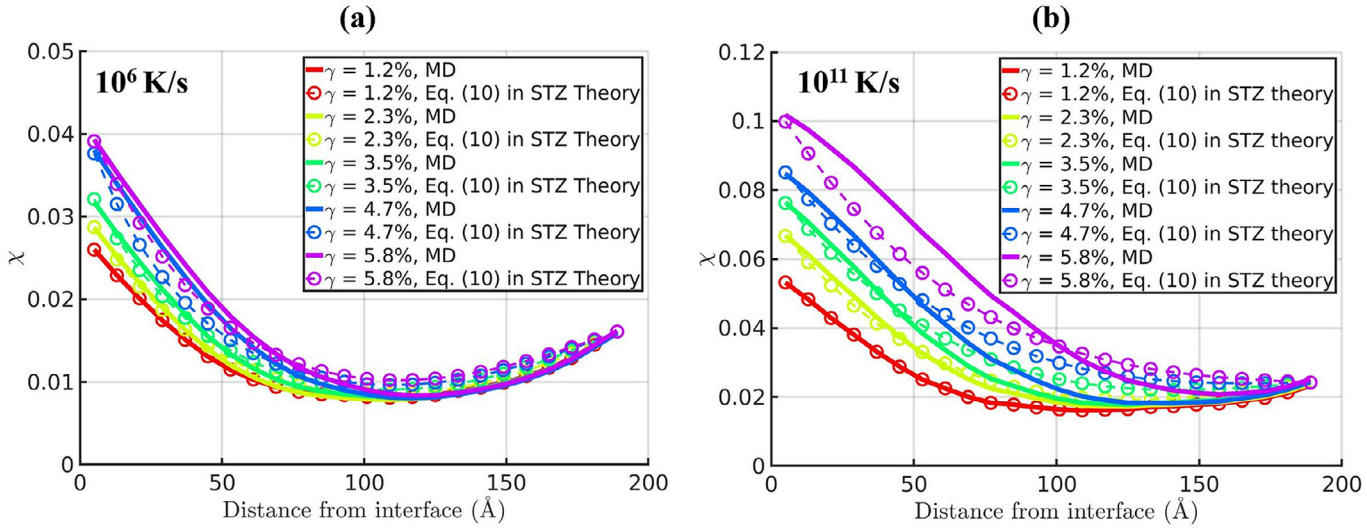

Fig. 10. The effective temperature diffusion, χ, across the $Cu_{64}Zr_{36}$ prepared under a cooling rate of (a) 10^6 K/s and (b) 10^{11} K/s. The solid curves are obtained from atomisitc simulations, and the dash lines with markers are the numerical solutions from the STZ theory using Eq. (10) where the atomistic data serves as the initial and boundary conditions.

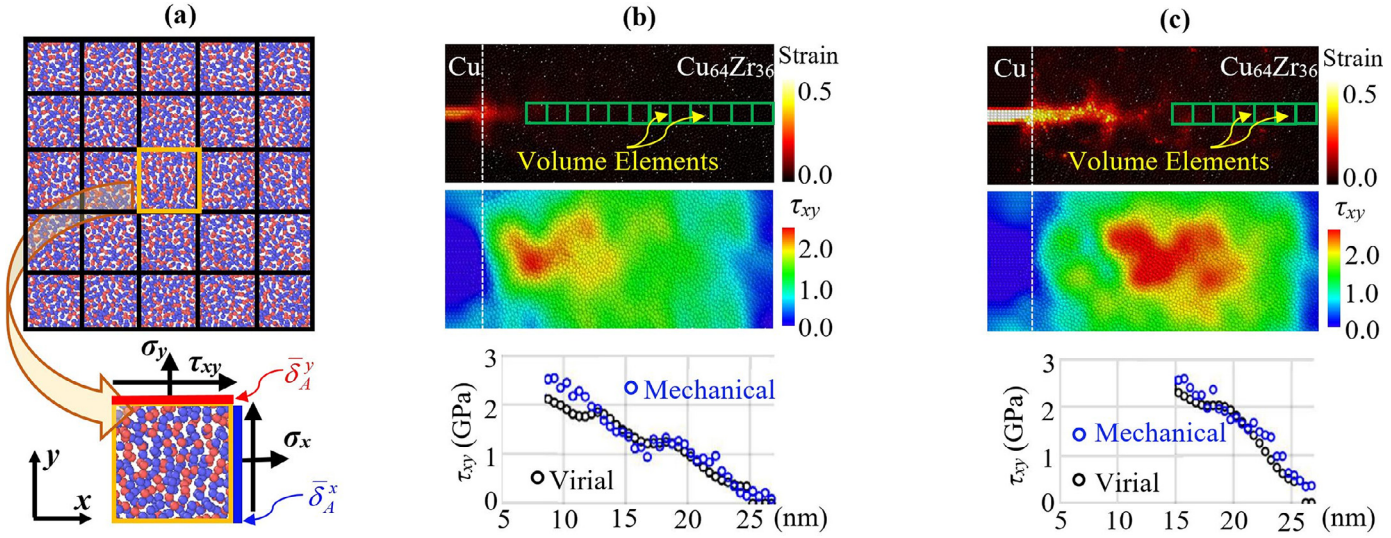

Fig. 11. The stress field ahead of the tip of the dislocation absorption-induced instability band in metallic glasses: (a) the set-up of the volume elements for the local stress measurements using Virial and a recently developed mechanical stress formula [34,35]; (b) when four and (c) nine dislocations are absorbed at the ACI.

The potential part, which is given in Eq. (12), is identical to the âmechanical stressâ defined by Cheung and Yip [32], i.e., the interatomic forces per unit area acting across a surface element. In this work, Eq. (12) is employed to quantify the local stress ahead of the dislocation absorption-induced instability in $Cu_{64}Zr_{36}$. Different from the atomic stress in crystalline materials, in which a local volume is associated with each single atom, the stress tensor in amorphous materials is usually obtained through a 'coarse-graining' procedure on different length scales using two most popular approaches: **(i)** introducing a 'coarse-graining' function, e.g., a Gaussian, to smooth the kinetic and potential contributions over a desired length scale [76]; and **(ii)** partitioning the simulation cell into multiple sub-volumes, and only those atoms residing in that volume contribute to the local stress tensor of the region [31]. In this work, the second approach is employed.

Firstly, we subdivide the $Cu_{64}Zr_{36}$ domain of the simulation cell into 1200 rectangular volume elements. Each volume element has a dimension of 0.5 nm $\times$ 0.5 nm in plane and contains $\sim$160 atoms. In order to evaluate the stress associated with each finite-sized volume element using Eq. (12), the total interatomic force across each face of the volume element is computed. Thereafter, the $\alpha\beta$th component of the stress tensor on the volume element is calculated as the αth component of the total force averaged by the area with its normal along the βth direction ($\alpha = 1,2,3;\ \beta = 1,2,3$). As an example, Fig. 11a shows a sketch of the mechanical stress components, σ_x, σ_y, and τ_{xy}, on a square element in a two-dimensional set-up. In this sketch, the area-average, $\overline{\delta}_A^{\beta}$, in Eq. (12) will be reduced to a length-average over element edges, noted as $\overline{\delta}_A^{x}$ and $\overline{\delta}_A^{y}$. By this way, the local stresses in volume elements containing different number of atoms can be measured. The obtained result can be compared against the Virial stress. The atomic strain distribution in Fig. 11b-c shows that a material instability band initiates at the dislocation-ACI intersection. This band then propagates along a plane of the maximum shear stress. In order to examine how the transient local stress state controls the material instability, here we plot the local shear stress distribution ahead of the tip of the instability band when four (Fig. 11b) and nine (Fig. 11c) dislocations are absorbed. It is seen that the instability of $Cu_{64}Zr_{36}$ creates a long-range ($\sim$15 nm) stress field ahead of the instability band. The local shear stress concentration at the tip of the instability band achieves a high level of $\sim$2.5 GPa. Such a high local stress may provide a driving force for the rapid growth of one dominant instability band.

The stress field induced by a localized irreversible event in solids is usually referred as an Eshelby field and decays by power laws. Fig. 11b, c show that the stress field ahead of the instability band is similar to the local stress field near a dislocation core or a crack tip, the former of which induces an r^{-1}-type while the latter induces an $r^{-1/2}$-type stress field. In Cu/$Cu_{64}Zr_{36}$ under a plastic shear, when multiple dislocations are absorbed at the same site, the local stress concentration can be much higher than the applied stress no matter the Virial or the mechanical stress formula is deployed. Also, consistent with our previous findings in [36], the atomic Virial stress (black circles in Fig. 11b, c) is found to underestimate the shear stress concentration comparing with that from the mechanical stress calculations (blue circles in Fig. 11b, c). One reason for such an underestimation is that a volume average always decreases the peak stress near a region where a fast change in the stress field occurs, e.g., the region close to a crack tip, a dislocation core, or the tip of an instability band. Moreover, we are aware of that, when the plastic strain carried by the dislocations is continuously transferred into the amorphous phase, the plastic flow in $Cu_{64}Zr_{36}$ is actually controlled by a multi-axial local stress state in general, rather than the applied shear stresses alone. The discussion to be presented in the following section will demonstrate that, the unique feature of the mechanical stress formula in recovering the full local Cauchy stress tensor enables us to accurately calibrate a thermodynamic-consistent criterion, e.g., a Mohr–Coulomb criterion [30]. This criterion can be used in a continuum-level model for detecting the instability in A/C-MCs under deformation.

3.5. *Calibration of the criterion for a local stress-controlled instability in glassy phases*

When dislocations are absorbed, the plastic strain carried by them are transmitted into the amorphous phase. It leads to the deformation of the glassy materials under a multi-axial stress. The continuous dislocation absorption at the same site of the ACI in Cu/$Cu_{64}Zr_{36}$ offers us an opportunity to characterize the local stress-controlled instability in A/C-MCs on the fly of the simulation. At the macroscopic level, the occurrence of the instability in metallic glasses is often described in terms of the Mohr–Coulomb criterion [30]. This criterion suggests that a glassy material yields under a combined shear and normal stresses, τ and σ. Mathematically, it is expressed as

$$\tau = \tau_0 - \alpha\sigma, \tag{13}$$

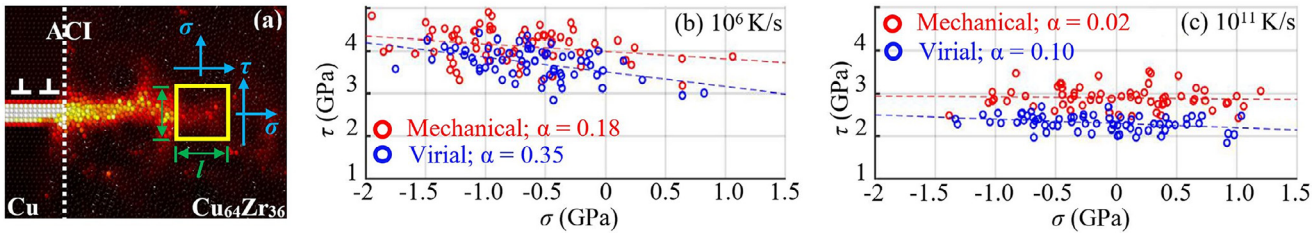

Fig. 12. Calibration of a criterion for detecting the metallic glass instability induced by a continuous dislocation absorptions at the ACI in Cu/$Cu_{64}Zr_{36}$ under a plastic shear: (a) the setup of a volume element for measuring the local shear and normal stress, τ and σ, ahead of the tip of an instability band; (b) the correlation between τ and σ ahead of the tip of an instability band in $Cu_{64}Zr_{36}$ prepared under a cooling rate of 10^6 K/s and (c) 10^{11} K/s.

where τ_0 is a critical shear stress at which the amorphous phase yields in the absence of any normal stress, and α is a friction coefficient that quantifies the effects of a normal stress on the yielding behavior. The form of Eq. (13) was originally developed for granular materials yielding, where the normal stress impedes the particle sliding with respect to each other. Hence, α represents an effective friction coefficient. When $\alpha = 0$, the Mohr-Coulomb criterion in Eq. (13) reduces to the widely-used Tresca criterion.

In order to examine the applicability of such a yielding criterion in detecting the local instability in glassy phases, during the continuous dislocation absorption, we measure the instantaneous local shear stress, τ, and also the local normal stress, σ, at the tip of an instability band (Fig. 12a).

The instability band tips are tracked through a threshold in the mean-squared non-affine atomic displacement. Ahead of the band tip, the volume element with an edge length of $l = 0.5$ nm is constructed (Fig. 12a). Corresponding to each dislocation absorption event, an instantaneous local stress state, τ and σ, are measured using the Virial and mechanical stress formula. Although the local stress fluctuation associated with the structural heterogeneity can be substantial, Fig. 12b, c show that the atomic shear stress, τ, approximately has a simple linear relationship to the normal stress, σ. Thus, the instantaneous local stress state obeys the functional form of the Mohr–Coulomb criterion. Linear fits to the scatter data of τ and σ capture the trend rather well. For the $Cu_{64}Zr_{36}$ prepared under a cooling rate of 10^6 K/s, the friction coefficients are found to be $\alpha = 0.18$ and $\alpha = 0.35$, respectively, when different formula are used for the local stress measurement (Fig. 12b).This is consistent with what has been found by Lund and Schuh in 2004 [77], who suggested a range of Mohr–Coulomb internal friction coefficient of $\alpha = 0.12$–0.40. We also notice that, comparing with the Virial formula, the deployment of a mechanical stress formula always produces a lower friction coefficient. More surprisingly, the friction coefficient extracted from the mechanical stress calculation agree with the macroscopic-level experimental results [78] reasonably better than that from the Virial stress calculation. In the same manner, we also investigate the dislocation absorption-induced instability in $Cu_{64}Zr_{36}$ prepared under a very high cooling rate of 10^{11} K/s. Fig. 12c presents the obtained τ–σ correlation. The friction coefficients in the Mohr–Coulomb criterion for such a super-cooled glassy phase can be calibrated as $\alpha = 0.02$ and $\alpha = 0.10$ when a mechanical and Virial stress formula are respectively used. These values are significantly lower than that, $\alpha = 0.18$ and $\alpha = 0.35$, in $Cu_{64}Zr_{36}$ prepared at the cooling rate of 10^6 K/s. Hence, the yielding of a "fast-cooled" $Cu_{64}Zr_{36}$ is mainly determined by the shear stresses while the effects of a normal stress are nearly negligible (Fig. 12c). The effects of normal stresses, σ, on the yielding behavior of metallic glasses are closely related to its processing history and microstructure: the lower cooling rates, the denser ICOs, and the larger friction coefficients. In other words, for a glassy phase prepared at a relatively low cooling rate, the slight increase/decrease of the tensile/compressive normal stress may significantly promote/suppress its instability.

The data presented in Fig. 12 show that the local shear and normal stresses, τ and σ, averaged over a finite-sized volume element satisfy the functional form of the Mohr–Coulomb criterion. However, it is not fully clear whether such a criterion will be valid on all the relevant length scales. To answer this question, here we investigate how the τ–σ correlation depends on the resolution, i.e., the dimension of the volume element, l, involved in the local stress measurement. We subdivide the $Cu_{64}Zr_{36}$ domain into cubic volume elements with two different sizes. One is in a dimension of $l = 0.5$ nm and the other is in a size of $l = 1.0$ nm. By this way, we can analyze the local stress states at different levels of 'coarse-graining' when the $Cu_{64}Zr_{36}$ is strained to the yielding point. When a mechanical stress formula is used, Fig. 13a shows that the stress data for both scales, $l = 0.5$ nm and $l = 1.0$ nm, falls along the straight lines and fits to the Mohr–Coulomb criterion with friction coefficients being $\alpha = 0.18$ and $\alpha = 0.15$, respectively. Similarly, an analysis of the scatter plots of τ and σ from the Virial stress calculations at $l = 0.5$ nm and $l = 1.0$ nm also shows that all data points fall onto straight lines but with different friction coefficients of $\alpha = 0.35$ and $\alpha = 0.30$ (Fig. 13b). No diverging from the linear $\tau - \sigma$ correlation has been observed at those two different length scales. The results imply that the Mohr-Coulomb criterion has a reasonable predictive power over plastic events in metallic glasses on length scales of 0.5 nm and above. However, it is observed that, when the resolution for the local stress measurement is reduced from $l = 1.0$ nm to $l = 0.5$ nm, the range of the stress fluctuation broadens (Fig. 13a, b). It is expected that the stress data for the smallest level of 'coarse-graining', i.e., a small volume element containing only a single

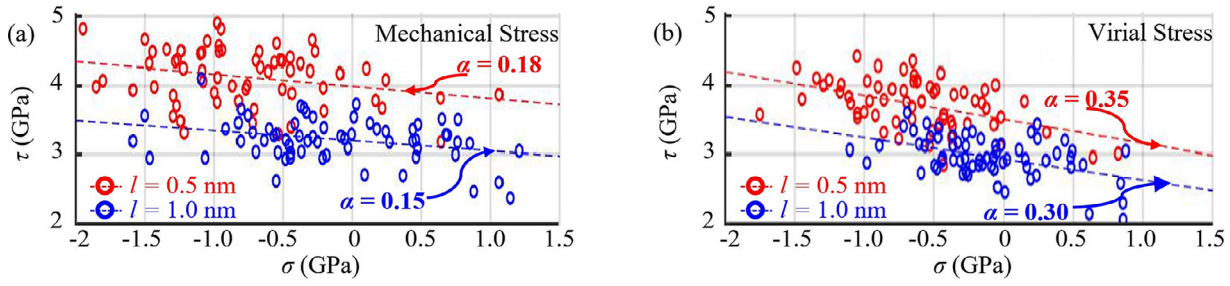

Fig. 13. Calibration of the resolution dependence of the friction coefficients, α, in the Mohr–Coulomb criterion for $Cu_{64}Zr_{36}$ (prepared under a cooling rate of 10^6 K/s) using (a) the mechanical and (b) the Virial stress formula.

or a few atoms, may scatter and largely deviate from a linear trend in the Mohr–Coulomb criterion. Although we are simulating the yielding of metallic glasses here, we believe this conclusion may be transferrable to a variety of amorphous solids, such as polymer glass or many other mixtures of particles interacting via Lennard–Jones or other short-range forces.

4. Summary and discussion

To summarize, through atomic-level computer simulations, here we attempt to build the connection between microstructure, plastic flow, local stress states, and yielding in a typical amorphous/crystalline metallic composite (A/C-MC), Cu/$Cu_{64}Zr_{36}$, on a firm atomistic basis. We gain insights into the atomic processes responsible for the co-deformation of crystalline and amorphous phases through:

(i) Characterizing the atomistic structure of the amorphous-crystalline interfaces (ACIs) in Cu/$Cu_{64}Zr_{36}$ prepared at different cooling rates ranging from an experimentally-comparable value of 10^4 K/s to 10^{13} K/s;
(ii) Probing the dislocation absorption-induced micro-structure evolution in Cu/$Cu_{64}Zr_{36}$ under deformation;
(iii) Correlating the number of the absorbed dislocation with the fraction of the activated STZs in $Cu_{64}Zr_{36}$;
(iv) Measuring the atomic-level local stress at the tip of a dislocation absorption-induced instability band.

Our several major findings are:

(a) The ICOs in $Cu_{64}Zr_{36}$ prepared at 10^{13} K/s are scattered, but form networks in $Cu_{64}Zr_{36}$ cooled at 10^4 K/s;
(b) The continuous dislocation absorption-induced instability in $Cu_{64}Zr_{36}$ occurs through a three-stage process, i.e., the STZ activation in between the ICOs, the coalescence of STZs, and the ICO fragmentation;
(c) The STZ formation energy in glassy phases is a decreasing function of the increasing cooling rates. In details, $E_z = 0.47$ eV and $E_z = 1.24$ eV for $Cu_{64}Zr_{36}$ prepared at 10^{11} K/s and 10^6 K/s, respectively;
(d) The number of the absorbed dislocations is correlated with the number of the atoms participating STZs.;
(e) The dislocation absorption-induced instability in $Cu_{64}Zr_{36}$ is controlled by the local stresses and is found to follow the Mohr–Coulomb criterion. The friction coefficient in the Mohr-Coulomb criterion depends on the material microstructure, the formula and also the resolution deployed in the local stress measurements.

Other than that, a connection between the above atomistic results and the effective temperature concept-based STZ theories has been also attempted through: (1) a direct measurement of the effective temperature, a key quantity in STZ theories, from atomistic simulations; (2) a correlation between the cooling rates, the effective temperature, and the dislocation absorption-induced shear band thickening, and a comparison of it with the STZ theory-based predictions; (3) a new formula of re-defining the effective temperature at the atomic scale by considering its dependence on the cooling rates; (4) the calibration of an effective temperature diffusion constant, which describes how fast the plasticity flows from crystalline to amorphous phases, and an incorporation of it into the STZ theory. By this way, the dislocation-interface reaction in A/C-MCs under deformation may be described as a diffusion of the effective temperature across the ACI; (5) a characterization of the shear transformation rate, $f(s)$, which is a function of the local stress and a key input of the STZ theory, from atomistic simulations, and examining its difference from the analytical form of $f(s)$. The above practices provide a preliminary guidance on how to calibrate the material models and the model parameters in a continuum-level STZ theory using the atomistic data; (6) the calibration of a single parameter, σ_0, which controls the amorphous materials bifurcation behavior in STZ theories, from an atomistic simulation-based $f(s)$.

These results may be utilized to achieve:

(1) A desirable smoother structure transition at the interface in Cu/$Cu_{64}Zr_{36}$ through combining Cu with $Cu_{64}Zr_{36}$ prepared at a lower cooling rate, in which the short-/medium-range order of the ICO structures in $Cu_{64}Zr_{36}$ gradually compromise with the long-range order in Cu near the amorphous/crystalline interface;
(2) A methodological manipulation of the three-stage deformation process through a fine control of the dislocation activities in Cu, the thermal processing history, or the chemical composition of the Cu_xZr_{1-x};
(3) A set of atomistic-informed constitutive relations, kinetic rules, and instability criterion that can be used in continuum-level computer models for predicting the mesoscopic-level microstructure evolution in plastically deformed A/C-MCs, where dislocations, STZs, and shear banding entangle with each other.

Although the atomistic analysis reveals insightful trends and sheds light on the mechanisms underlying the deformation behavior in A/C-MC subjected to a mechanical loading. Before concluding this paper, we shall point out that the present simulations do not reproduce all the details about the dislocation-interface reactions in A/C-MCs under deformation. On one hand, when an A/C-MC is subjected to a loading, there indeed exist two possibilities: (i) the crystalline; or (ii) the amorphous phase, deforms first. For the first situation, the major concern will be: how the amorphous phase accommodates the plastic flow when the dislocations generated in crystalline phases arrive at the ACI? This is also the primary focus of the present work. For the second situation, the major concern becomes: how the crystalline layer accommodates plastic deformation when the shear band generated in amorphous phase reaches the ACI? We are aware of the importance of this topic, and have recently performed a series of atomistic simulations of tri-layered Cu/CuZr/Cu under deformation. Our preliminary results show that, when the shear band arrives at an ACI, it may trigger simultaneous dislocation nucleation on multiple adjacent slip planes in a Cu layer due to the finite width of a shear band. We believe that the interaction between a shear band and the ACI deserves an extensive and comprehensive research in a separate manuscript, and thus do not include it into the present work at this stage. On the other hand, the atomic-level computer simulations should never be considered to be perfectly sufficient in determining a truly general processing-structure-property relationship for such a complex material system. We have no doubt that some of our observations here might not be exactly the same as that in reality due to the artifacts induced by the computational set-up. In particular, atomistic simulations are limited in length scales. The small simulation cells may suppress the relevant larger-scale features of a dislocation absorption-induced instability in real-word A/C-MCs. Although the dislocations most likely will not pile up at the ACI because they can be easily absorbed by the amorphous phases, the long-range stress or strain gradient associated with those dislocations approaching the ACI may still play important roles in the STZ percolation. As such, despite of its power in revealing the atomic-level deformation mechanisms, the atomistic simulation presented here are not intended to reproduce all the exact experimental observations. Mapping the computationally-revealed mechanisms to the experimentally-observed behavior of A/C-MCs necessitates a multi-scale computational framework that can span several disparate lengths scales ranging from angstroms, to nanometers, microns and even above.

We argue that our recently developed concurrent atomistic-continuum (CAC) method [79–85], if not the best, may provide an

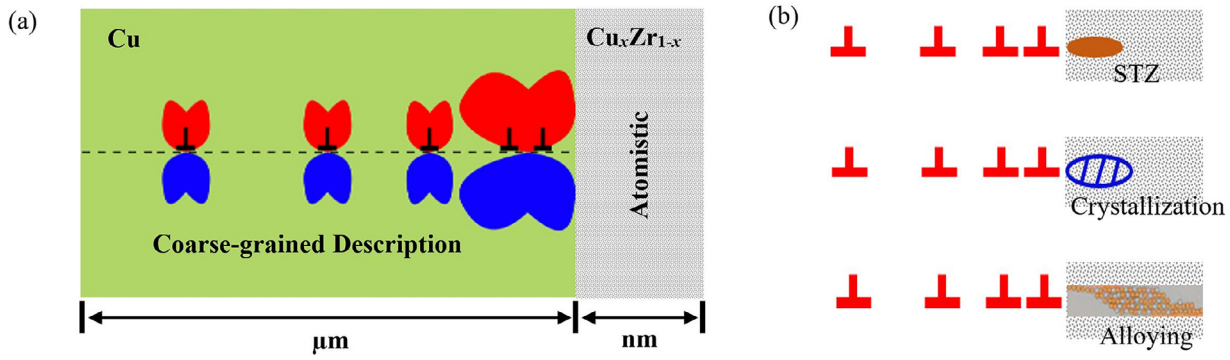

Fig. 14. (a) A sketch of CAC for modeling the Cu/Cu_xZr_{1-x} from the atomistic to the microscale; (b) a variety of mechanisms for the interactions between dislocations and the ACI [14–22].

alternative strategy of scaling up in lengths for modeling the plastic flow in A/C-MCs. Fundamental to the CAC method is an atomistic field formulation that unifies the atomistic and continuum description of materials [72,86]. This formulation generalizes Kirkwoodâs statistical theory of transport processes [73–75] by including a two-level description of crystalline materials. Those equations in this formulation are identical in form to the differential equation in continuum mechanics. Thus, continuum modeling techniques, such as finite element (FE), can be used to solve for the atomic displacement field. The utilization of coarse elements in regions where the material deforms cooperatively leads to a coarse-grained (CG) atomistic description of materials [87,88]. Distinct from the effective temperature-based description of dislocations in [70], the CG model can explicitly retain the atomistic core structures of micrometer-long dislocation lines at a significantly less cost than that by a fully atomistic model. CG was demonstrated to be successful in capturing the complex dislocation activities in a broad range of metallic materials at the micrometer level [87,88].

The combination of CG and atomistic results in a CAC model. One main novelty of CAC is to bridge the relevant length scales through resolving the material interface at an atomistic resolution while the lagging dislocations away from the interface in a CG description (Fig. 14). Such a computer model is multiscale in nature and was shown to be effective in predicting the reactions between a sequential dislocation and the grain boundaries in metallic materials from the atomistic to the sub-micron level [81]. These results demonstrate that CAC has a potential to be applicable to characterize the interplay between the long-range dislocation-mediated plastic flow and the atomic-scale interface structure evolution in amorphous/crystalline metallic composites. It will expand the atomistic-simulation-based predictive capability from nanometers to micrometers and may enable us to test one hypothesis: with a fine control of the applied plastic shear strain at the macroscopic level and the interface structure at the nanoscale, the dislocation-ACI reaction might be manipulated. A manipulation of the coupled dynamics between dislocations and STZs, if succeed, may allow us to not only suppress the STZ-induced instability, but also promote the synergy of several other mechanisms, such as crystallization or alloying [14–22] (Fig. 14b), to further toughen this material system. The test of this hypothesis will be conducted and reported in our future work. The gained knowledge is expected to provide the support for a rational design of simultaneously strong and tough materials applied in a variety of safety-critical engineering infrastructures.

Declaration of competing interest

The authors declare that they have no known competing financial interests or personal relationships that could have appeared to influence the work reported in this paper.

Acknowledgments

TC, AB, and LX acknowledge the support of US National Science Foundation (NSF) with an award number of DMR-1807545 and the Extreme Science and Engineering Discovery Environment (XSEDE-TG-MSS170003). JR and LX also acknowledge the support from NSF through the project of CMMI-1536925.The work of YC is supported by NSF with an award number of CMMI-1761512. A discussion with Dr. Michael Falk at Johns Hopkins University on informing the obtained atomistic data into the STZ theory is also greatly appreciated.

References

[1] H. Gleiter, Nanocrystalline materials, Prog. Mater. Sci. 33 (1989) 223–315.
[2] H. Gleiter, Nanostructured materials: basic concepts and microstructure, Acta Mater. 48 (1) (2000) 1–29.
[3] Y. Wang, M. Chen, F. Zhou, E. Ma, High tensile ductility in a nanostructured metal, Nature 419 (6910) (2002) 912.
[4] M.A. Meyers, A. Mishra, D.J. Benson, Mechanical properties of nanocrystalline materials, Prog. Mater. Sci. 51 (4) (2006) 427–556.
[5] L. Lu, Y. Shen, X. Chen, L. Qian, K. Lu, Ultrahigh strength and high electrical conductivity in copper, Science 304 (5669) (2004) 422–426.
[6] L. Lu, X. Chen, X. Huang, K. Lu, Revealing the maximum strength in nanotwinned copper, Science 323 (5914) (2009) 607–610.
[7] T. Zhu, J. Li, A. Samanta, H.G. Kim, S. Suresh, Interfacial plasticity governs strain rate sensitivity and ductility in nanostructured metals, Proc. Natl. Acad. Sci. USA 104 (9) (2007) 3031–3036.
[8] A. Misra, R. Hoagland, H. Kung, Thermal stability of self-supported nanolayered Cu/Nb films, Philos. Mag. 84 (10) (2004) 1021–1028.
[9] I.J. Beyerlein, N.A. Mara, J. Wang, J.S. Carpenter, S.J. Zheng, W.Z. Han, R.F. Zhang, K. Kang, T. Nizolek, T.M. Pollock, Structure-property-functionality of bimetal interfaces, JOM 64 (2012) 1192.
[10] I.J. Beyerlein, N.A. Mara, J.S. Carpenter, T. Nizolek, W.M. Mook, T.A. Wynn, R.J. McCabe, J.R. Mayeur, K. Kang, S. Zheng, J. Wang, T.M. Pollock, Interface-driven microstructure development and ultra high strength of bulk nanostructured Cu-Nb multilayers fabricated by severe plastic deformation, J. Mater. Res. 28 (2013) 1799–1812.
[11] I.J. Beyerlein, J.R. Mayeur, S. Zheng, N.A. Mara, J. Wang, A. Misra, Emergence of stable interfaces under extreme plastic deformation, Proc. Natl. Acad. Sci. USA 111 (2013) 4386–4390.
[12] J. Sun, B. Bhushan, Hierarchical structure and mechanical properties of nacre: a review, RSC Adv. 2 (2012) 7617–7632.
[13] L.M. Gordon, M.J. Cohen, K.W. MacRenaris, J.D. Pasteris, T. Seda, D. Joester, Amorphous intergranular phases control the properties of rodent tooth enamel, Science 347 (2015) 746–750.
[14] A. Donohue, F. Spaepen, R.G. Hoagland, A. Misra, Suppression of the shear band instability during plastic flow of nanometer-scale confined metallic glasses, Appl. Phys. Lett. 91 (2007) 241905.
[15] Y. Wang, J. Li, A.V. Hamza, T.W. Barbee, Ductile crystalline-amorphous nanolaminates, Proc. Natl. Acad. Sci. USA 104 (2007) 11155–11160.
[16] A. Khalajhedayati, Z. Pan, T.J. Rupert, Manipulating the interfacial structure of nanomaterials to achieve a unique combination of strength and ductility, Nat. Commun. 7 (2016) 10802.
[17] Y.Q. Wang, J.Y. Zhang, X.Q. Liang, K. Wu, G. Liu, J. Sun, Size-and constituent-dependent deformation mechanisms and strain rate sensitivity in nanolaminated crystalline cu/amorphous cu–Zr films, Acta Mater. 95 (2015) 132–144.
[18] J.Y. Zhang, G. Liu, S.Y. Lei, J.J. Niu, J. Sun, Transition from homogeneous-like to shear-band deformation in nanolayered crystalline Cu/amorphous Cu-Zr micropillars: intrinsic vs. extrinsic size effect, Acta Mater. 60 (20) (2012) 7183–7196.
[19] J.Y. Zhang, G. Liu, J. Sun, Crystallization-aided extraordinary plastic deformation in nanolayered crystalline Cu/amorphous Cu-Zr micropillars, Sci. Rep. 3 (2013) 2324.

[20] J.Y. Zhang, G. Liu, J. Sun, Self-toughening crystalline Cu/amorphous Cu-Zr nanolaminates: deformation-induced devitrification, Acta Mater. 66 (2014) 22–31.
[21] J.Y. Zhang, Y.Q. Wang, X.Q. Liang, F.L. Zeng, G. Liu, J. Sun, Size-dependent he-irradiated tolerance and plastic deformation of crystalline/amorphous Cu/Cu–Zr nanolaminates, Acta Mater. 92 (2015) 140–151.
[22] W. Guo, E. Jägle, J. Yao, V. Maier, S. Korte-Kerzel, J.M. Schneider, D. Raabe, Intrinsic and extrinsic size effects in the deformation of amorphous CuZr/nanocrystalline Cu nanolaminates, Acta Mater. 80 (2014) 94–106.
[23] F. Abdeljawad, M. Haataja, Continuum modeling of bulk metallic glasses and composites, Phys. Rev. Lett. 105 (12) (2010) 125503.
[24] G.P. Zheng, Application of phase-field modeling to deformation of metallic glasses, Curr. Opin. Solid State Mater. Sci. 15 (3) (2011) 116–124.
[25] Z. Pan, T.J. Rupert, Spatial variation of short-range order in amorphous intergranular complexions, Comput. Mater. Sci. 131 (2017) 62–68.
[26] B. Cheng, J.R. Trelewicz, Mechanistic coupling of dislocation and shear transformation zone plasticity in crystalline-amorphous nanolaminates, Acta Mater. 117 (2016) 293–305.
[27] Y. Cui, O.T. Abad, F. Wang, P. Huang, T.J. Lu, K.W. Xu, J. Wang, Plastic deformation modes of CuZr/Cu multilayers, Sci. Rep. 6 (2016) 23306.
[28] Z. Pan, T.J. Rupert, Amorphous intergranular films as toughening structural features, Acta Mater. 89 (2015) 205–214.
[29] V. Turlo, T.J. Rupert, Grain boundary complexions and the strength of nanocrystalline metals: dislocation emission and propagation, Acta Mater. 151 (2018) 100–111.
[30] C.A. Schuh, A.C. Lund, Atomistic basis for the plastic yield criterion of metallic glass, Nat. Mater. 2 (7) (2003) 449.
[31] D. MacNeill, J. Rottler, From macroscopic yield criteria to atomic stresses in polymer glasses, Phys. Rev. E 81 (1) (2010) 011804.
[32] K.S. Cheung, S. Yip, Atomic-level stress in an inhomogeneous system, J. Appl. Phys. 70 (10) (1991) 5688–5690.
[33] W.D. Hoover, 1, Elsevier, Amsterdam, The Netherlands, 1991.
[34] Y. Chen, The origin of the distinction between microscopic formulas for stress and Cauchy stress, EPL 116 (3) (2016) 34003.
[35] Y. Chen, A. Diaz, Local momentum and heat fluxes in transient transport processes and inhomogeneous systems, Phys. Rev. E 94 (5) (2016) 053309.
[36] J. Rigelesaiyin, A. Diaz, W. Li, L. Xiong, Y. Chen, Asymmetry of the atomic-level stress tensor in homogeneous and inhomogeneous materials, Proc. Royal Soc. Lond. A 474 (2217) (2018) 20180155.
[37] D. Xu, B. Lohwongwatana, G. Duan, W.L. Johnson, C. Garland, Bulk metallic glass formation in binary Cu-rich alloy series-$Cu_{100-x}Zr_x$ ($x = 34, 36, 38.2, 40$ at.%) and mechanical properties of bulk $Cu_{64}Zr_{36}$ glass, Acta Mater. 52 (9) (2004) 2621–2624.
[38] D. Arias, J.P. Abriata, The Cu-Zr (Copper-Zirconium) system, Bull. Alloy Phase Diagrams 11 (5) (1990) 452–459.
[39] M.W. Finnis, J.E. Sinclair, A simple empirical N-body potential for transition metals, Phil. Mag. A 50 (1) (1984) 45–55.
[40] M.I. Mendelev, M.J. Kramer, R.T. Ott, D.J. Sordelet, Molecular dynamics simulation of diffusion in supercooled Cu-Zr alloys, Phil. Mag. 89 (2) (2009) 109–126.
[41] M.S. Daw, M.I. Baskes, Semiempirical, quantum mechanical calculation of hydrogen embrittlement in metals, Phys. Rev. Lett. 50 (17) (1983) 1285.
[42] Y.Q. Cheng, H.W. Sheng, E. Ma, Relationship between structure, dynamics, and mechanical properties in metallic glass-forming alloys, Phys. Rev. B 78 (1) (2008) 014207.
[43] Y.Q. Cheng, E. Ma, H.W. Sheng, Atomic level structure in multicomponent bulk metallic glass, Phys. Rev. Lett. 102 (24) (2009) 245501.
[44] S. Plimpton, Fast parallel algorithms for short-range molecular dynamics, J. Comp. Phys. 117 (1) (1995) 1–19.
[45] (https://lammps.sandia.gov/).
[46] Y. Zhang, F. Zhang, C.Z. Wang, M.I. Mendelev, M.J. Kramer, K.M. Ho, Cooling rates dependence of medium-range order development in $Cu_{64.5}Zr_{35.5}$ metallic glass, Phys. Rev. B 91 (6) (2015) 064105.
[47] Y. Sun, Y. Zhang, F. Zhang, Z. Ye, Z. Ding, C.Z. Wang, K.M. Ho, Cooling rate dependence of structural order in $Al_{90}Sm_{10}$ metallic glass, J. Appl. Phys. 120 (1) (2016) 015901.
[48] T. Wen, Y. Sun, B. Ye, L. Tang, Z. Yang, K.M. Ho, C.Z. Wang, N. Wang, Cooling rate dependence of structural order in $Ni_{62}Nb_{38}$ metallic glass, J. Appl. Phys. 123 (4) (2018) 045108.
[49] J.L. Finney, Random packings and the structure of simple liquids. i. The geometry of random close packing, Proc. Royal Soc. Lond. A 319 (1539) (1970) 479–493.
[50] J.L. Finney, Modelling the structures of amorphous metals and alloys, Nature 266 (5600) (1977) 309.
[51] V.A. Borodin, Local atomic arrangements in polytetrahedral materials, Phil. Mag. A 79 (8) (1999) 1887–1907.
[52] V.A. Borodin, Local atomic arrangements in polytetrahedral materials II. Coordination polyhedra with 14 and 15 atoms, Philos. Mag. A 81 (10) (2001) 2427–2446.
[53] F.C. Frank, Supercooling of liquids, Proc. Royal Soc. Lond. A 215 (1120) (1952) 43–46.
[54] Y.Q. Cheng, A.J. Cao, H.W. Sheng, E. Ma, Local order influences initiation of plastic flow in metallic glass: effects of alloy composition and sample cooling history, Acta Mater. 56 (18) (2008) 5263–5275.
[55] C. Brandl, T.C. Germann, A. Misra, Structure and shear deformation of metallic crystalline-amorphous interfaces, Acta Mater. 61 (10) (2013) 3600–3611.
[56] S. Scudino, D. Şopu, Strain distribution across an individual shear band in real and simulated metallic glasses, Nano Lett. 18 (2) (2018) 1221–1227.
[57] A. Stukowski, Visualization and analysis of atomistic simulation data with OVITO–the open visualization tool, Model. Simul. Mater. Sci. Eng. 18 (1) (2009) 015012.
[58] D. Şopu, A. Stukowski, M. Stoica, S. Scudino, Atomic-level processes of shear band nucleation in metallic glasses, Phys. Rev. Lett. 119 (19) (2017) 195503.
[59] J. Ding, S. Patinet, M.L. Falk, Y. Cheng, E. Ma, Soft spots and their structural signature in a metallic glass, Proc. Natl. Acad. Sci. U.S.A. 111 (39) (2014) 14052–14056.
[60] V.I. Levitas, O.M. Zarechnyy, Kinetics of strain-induced structural changes under high pressure, J. Phys. Chem. B 110 (32) (2006) 16035–16046.
[61] V.I. Levitas, High-pressure mechanochemistry: conceptual multiscale theory and interpretation of experiments, Phys. Rev. B 70 (18) (2004) 184118.
[62] N.A. Zarkevich, H. Chen, V.I. Levitas, D.D. Johnson, Lattice instability during solid-solid structural transformations under a general applied stress tensor: example of si i → si II with metallization, Phys. Rev. Lett. 121 (16) (2018) 165701.
[63] D.D. Alix-Williams, M.L. Falk, Shear band broadening in simulated glasses, Phys. Rev. E 98 (5) (2018) 053002.
[64] D.H. Tsai, The virial theorem and stress calculation in molecular dynamics, J. Chem. Phys. 70 (3) (1979) 1375–1382.
[65] A. Torres-Sánchez, J.M. Vanegas, M. Arroyo, Examining the mechanical equilibrium of microscopic stresses in molecular simulations, Phys. Rev. Lett. 114 (25) (2015) 258102.
[66] M. Zhou, A new look at the atomic level virial stress: on continuum-molecular system equivalence, Proc. Royal Soc. Lond. A 459 (2037) (2003) 2347–2392.
[67] A.R. Hinkle, C.H. Rycroft, M.D. Shields, M.L. Falk, Coarse graining atomistic simulations of plastically deforming amorphous solids, Phys. Rev. E 95 (5) (2017) 053001.
[68] M.L. Manning, J.S. Langer, J.M. Carlson, Strain localization in a shear transformation zone model for amorphous solids, Phys. Rev. E 76 (5) (2007) 056106.
[69] M.L. Manning, E.G. Daub, J.S. Langer, J.M. Carlson, Rate-dependent shear bands in a shear-transformation-zone model of amorphous solids, Phys. Rev. E 79 (1) (2009) 016110.
[70] M.Y. Tong, C.K.C. Lieou, I.J. Beyerlein, Deformation profile and interface-mediated defect interaction in Cu/CuZr nanolaminates: an effective-temperature description, Phys. Rev. Mater. 3 (7) (2019) 073602.
[71] J.A. Zimmerman, E.B. Webb III, J.J. Hoyt, R.E. Jones, P.A. Klein, D.J. Bammann, Calculation of stress in atomistic simulation, Model. Simul. Mater. Sci. Eng. 12 (4) (2004) S319.
[72] Y. Chen, Reformulation of microscopic balance equations for multiscale materials modeling, J. Chem. Phys. 130 (13) (2009) 134706.
[73] J.G. Kirkwood, The statistical mechanical theory of transport processes I. General theory, J. Chem. Phys. 14 (3) (1946) 180–201.
[74] J.G. Kirkwood, The statistical mechanical theory of transport processes II. Transport in gases, J. Chem. Phys. 15 (1) (1947) 72–76.
[75] J.H. Irving, J.G. Kirkwood, The statistical mechanical theory of transport processes. IV. The equations of hydrodynamics, J. Chem. Phys. 18 (6) (1950) 817–829.
[76] I. Goldhirsch, C. Goldenberg, On the microscopic foundations of elasticity, Eur. Phys. J. E 9 (cond-mat/0203360) (2002) 245.
[77] A.C. Lund, C.A. Schuh, The mohr–Coulomb criterion from unit shear processes in metallic glass, Intermetallics 12 (10–11) (2004) 1159–1165.
[78] X. Lei, Y. Wei, B. Wei, W.H. Wang, Spiral fracture in metallic glasses and its correlation with failure criterion, Acta Mater. 99 (2015) 206–212.
[79] L. Xiong, Q. Deng, G. Tucker, D.L. McDowell, Y. Chen, A concurrent scheme for passing dislocations from atomistic to continuum domains, Acta Mater. 60 (3) (2012) 899–913.
[80] L. Xiong, S. Xu, D.L. McDowell, Y. Chen, Concurrent atomistic–continuum simulations of dislocation–void interactions in fcc crystals, Int. J. Plast. 65 (2015) 33–42.
[81] S. Xu, L. Xiong, Y. Chen, D.L. McDowell, Sequential slip transfer of mixed-character dislocations across $\sigma 3$ coherent twin boundary in fcc metals: a concurrent atomistic-continuum study, NPJ Comput. Mater. 2 (2016) 15016.
[82] S. Xu, T.G. Payne, H. Chen, Y. Liu, L. Xiong, Y. Chen, D.L. McDowell, PyCAC: the concurrent atomistic-continuum simulation environment, J. Mater. Res. 33 (7) (2018) 858.
[83] X. Chen, A. Diaz, L. Xiong, D.L. McDowell, Y. Chen, Passing waves from atomistic to continuum, J. Comp. Phys. 354 (2018) 393–402.
[84] X. Chen, W. Li, L. Xiong, Y. Li, S. Yang, Z. Zheng, D.L. McDowell, Y. Chen, Ballistic-diffusive phonon heat transport across grain boundaries, Acta Mater. 136 (2017) 355–365.
[85] L. Xiong, X. Chen, N. Zhang, D.L. McDowell, Y. Chen, Prediction of phonon properties of 1D polyatomic systems using concurrent atomistic–continuum simulation, Arch. Appl. Mech. 84 (2014) 1665–1675.
[86] Y. Chen, Reformulation of microscopic balance equations for multiscale materials modeling, J. Chem. Phys. 130 (13) (2009) 134706.
[87] L. Xiong, G. Tucker, D.L. McDowell, Y. Chen, Coarse-grained atomistic simulation of dislocations, J. Mech. Phys. Solids 59 (2) (2011) 160–177.
[88] L. Xiong, D.L. McDowell, Y. Chen, Sub-THz phonon drag on dislocations by coarse-grained atomistic simulations, Int. J. Plast. 55 (2014) 268–278.